Case Studies in Construction Materials 22 (2025) e04064

Contents lists available at ScienceDirect

Case Studies in Construction Materials

journal homepage: www.elsevier.com/locate/cscm

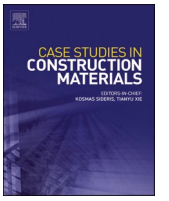

Case study

A case study on the impact of fiber distribution on X-connections of complex-shaped UHPFRC footbridges cast with recyclable formwork

Duc Anh Tran [a], Sandrine Heroux [b], Luca Sorelli [a,*], Mahdi Ben Ftima [c], David Conciatori [a], Christian Dupuis [d], Samuel Bernier-Lavigne [b]

[a] Université Laval, Department of Civil and Water Engineering, Canada
[b] Université Laval, École d'architecture, Canada
[c] Polytechnique of Montreal, Department of Civil and Water Engineering, Canada
[d] Université Laval, Department of Geology and Geological Engineering, Canada

ARTICLE INFO

Keywords:
UHPFRC
Fiber distribution
Fiber orientation
Multiple cracking
Digital Image Correlation
Magnetic inductance method
Recyclable formwork
Non linear finite element analysis

ABSTRACT

Ultra-High Performance Fiber Reinforced Concrete (UHPFRC) is emerging as a transformative construction material, enabling the creation of slender, thin architectural structures with outstanding surface textures. This study examines the influence of fiber distribution on the mechanical behavior of the X-connection, a critical structural detail in a novel latticework concept for UHPFRC footbridges, while also introducing an innovative approach using recycled wax formwork for shaping complex geometries.

Following the architectural design process for the latticework UHPFRC footbridge, the methodology involves: (i) fabrication of fully recyclable wax formwork using CNC milling for two X-connection configurations with distinct crossing angles (i.e., the angle formed at the intersection of the X shape); (ii) gravity casting of UHPFRC, incorporating 1 % steel microfibers; (iii) application of the magnetic inductance method (MIM) for non-destructive testing to evaluate fiber distribution, supplemented by fiber counting and image analysis of cracked sections post-testing; (iv) mechanical testing of the X-connection under bending to assess structural performance; and (v) a nonlinear Finite Element Analysis (NLFEA) to comprehensively examine the impact of fiber distribution. The findings underscore the pivotal role of fiber distribution in determining the ductility and strength of X-connections within the latticework UHPFRC footbridge, elucidating both the strengths and constraints of contemporary magnetic methods integrated with the Finite Element Method for accurately predicting the effects of fiber distribution.

1. Introduction

Ultra-High Performance Fiber Reinforced Concrete (UHPFRC) is increasingly utilized worldwide for its superior adaptability in crafting architecturally complex structures, such as the perforated latticework of the station roofing of Montpellier [1], the perforated triangular elements of Jean-Bouin [2], as well as the randomized fishnet of Mucem museum [3,4] as well as lattice perforated architectural panels with possible complexes arabesque geometry [5]. Fig. 1 shows the exponential trend in the citations and

* Corresponding author.
E-mail address: luca.sorelli@gci.ulaval.ca (L. Sorelli).

https://doi.org/10.1016/j.cscm.2024.e04064
Received 23 September 2023; Received in revised form 3 November 2024; Accepted 1 December 2024
Available online 9 December 2024

List of Symbols

Latin upper case

A_f	Area of the cross-section of a fiber (mm^2)
K	Coefficient of dispersion on fiber orientation
K_{local}	Coefficient of dispersion localization on fiber orientation
K_{Global}	Coefficient of dispersion global on fiber orientation
L_{air}	The inductance measurement in the air
L_X	The inductance measurement on direction X
L_Y	The inductance measurement on direction Y
V_f	The fiber volume fraction (%)
M_{max}	The ultimate flexural strength at the fracture point (MPa)
$M_{max}^{unif\_\mu_0=0.5}$	The average flexural strength of the reference beam (MPa)
M_{max}^{exp}	The flexural strength of each beam (MPa)
W^*	Energy dissipated up to 7 mm of deflection (J)

Latin lower case

d_{f1}	The length of the major axes (mm)
d_{f2}	The length of the minor axes (mm)
f_{Ute}	The strength of tensile at the elastic point (MPa)
f_{Utu}	The strength of tensile at the ultimate point (MPa)
n_f	The number of fibers intercepting the localized crack

Greek lower case

ϵ	Eccentricity (the default value 0.1) - CDP model
θ	the orientation angle (°)
μ	1. The viscosity parameter represents the relaxation time of the viscoplastic system. (CDP model) 2. The magnetic permeability (MIM)
μ_0	The orientation factors of fibers
$\mu_{0,i}$	The fiber orientation factor direction I
μ_0^{IA}	The orientation factors of fibers by image analysis
μ_0^{MIM}	The orientation factors of fibers by MIM
μ_1	The efficiency factors of fibers
$\mu_{1,i}$	The efficiency factors of fibers direction I
$\mu_{r,mean}$	The mean relative magnetic permeability
$\mu_{r,X}$	The relative magnetic permeability in direction X
$\mu_{r,Y}$	The relative magnetic permeability in direction Y
υ	Coefficient Poisson
$\rho_X - \rho_Y$	Fiber orientation indicator
σ_{b0}	Initial equiaxial compressive yield stress (MPa)
σ_{c0}	Initial uniaxial compressive yield stress (MPa)
φ	Orientation of the fiber with respect to the cracking plan (°)
φ_0	Angle between the average orientation of the fibers and the main direction of traction
ψ	The dilation angle measured in the p-q plane at high confining pressure

publications of journal articles with keywords UHPFRC and architecture.

The exceptional mechanical properties of UHPFRC enable the design of unprecedented structural shapes. Indeed, UHPFRC structures reinforced with short steel micro-fibers, serving as an alternative to steel rebars, facilitate greater design flexibility and enable the realization of more free-form shapes [7,8]. However, the distribution of steel fibers can strongly affect the flexural and tensile response of UHPFRC elements as shown by landmark works [9,10]. As for tensile test on UHPFRC, Bayard demonstrated that varying the orientation of steel fibers from parallel to perpendicular to the tensile load direction can reduce tensile strength and ductility by approximately a factor of 3, and fracture energy by a factor of 4 [9]. In bending tests on UHPFRC, Bernier et al. discovered that flexural strength can also be reduced by a factor of 3 by varying the fiber orientation from favorable to unfavorable directions [10]. Thus, fiber distribution is critical in scenarios where the casting process could result in uneven fiber distribution in essential zones. In the case of the Jean-Bouin project, the orientation of fibers within the "branches" (identified as X-connections) were carefully examined due to the risk of weak or cold joints at the nodes due to possible filling and joining concrete flows. Cold joints may strongly reduce the mechanical performance of UHPC panel and increasing their risk of cracking [11]. When filling complex molds with multiple pathways and intersecting nodes, there is a possibility for fresh concrete flows to converge at nodes, creating cold joints or

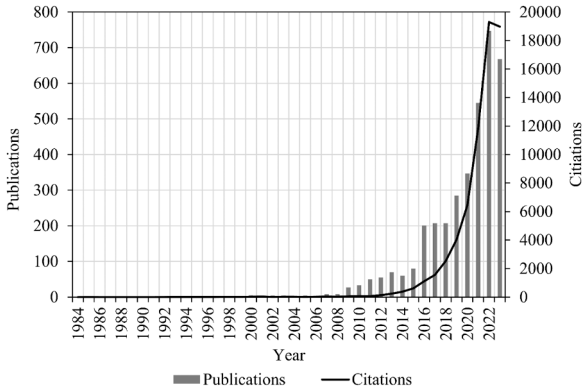

Fig. 1. Number of publications and citation with keywords UHPFRC and architecture from Web of Science [6].

weak zones with low fiber content [11].

French recommendations defined a K-factor for taking into account the effect of fiber distribution [12]. A K-factor superior to 2 (that is, 50 % of expected fiber) was observed in connection nodes in previous works even when considering high quality control efforts [12]. Lattice UHPFRC architecture necessitates then a meticulous examination of the effects of fiber distribution in the nodes to ensure the required strength and the minimum ductility for redistributing internal forces and assuring reliability. The challenge lies in minimizing the volume content of steel microfiber, which are costly, while still ensuring the necessary ductility in connections to support the structure's hyperstatic demands [13].

Nunes at al. developed a non-destructive method based on magnetic inductance has been developed to assess the fiber distribution for thin UHPFRC elements [14]. MIM method was found to be reliable in measuring the spatial distribution of the fiber volume and orientation for UHPFRC element on rectangular beam [15], dumbbell specimen [16], and UHPFRC layer [17]. The MIM method is also referenced in the Swiss code SIA 2052 for quality control of UHPFRC elements [18]. Moreover, Tran et al. [19] employed the MIM measurements with a numerical model to predict the tensile behavior of UHPC prismatic element in tension, confirming the importance of considering the effective fiber distribution in the interpretation of the tensile response.

UHPC architecture with complex shapes can take advantage of new digital fabrication technologies [20,21]. Here we propose the study of an architectural element made of ultra-high performance fiber reinforced concrete. It is apart from the ideal of the footbridge in Quebec City (Fig. 2) [22]. One of the inherent challenges for casting complex shape structure made of self-compacting UHPC may be the cost of the formwork [23].

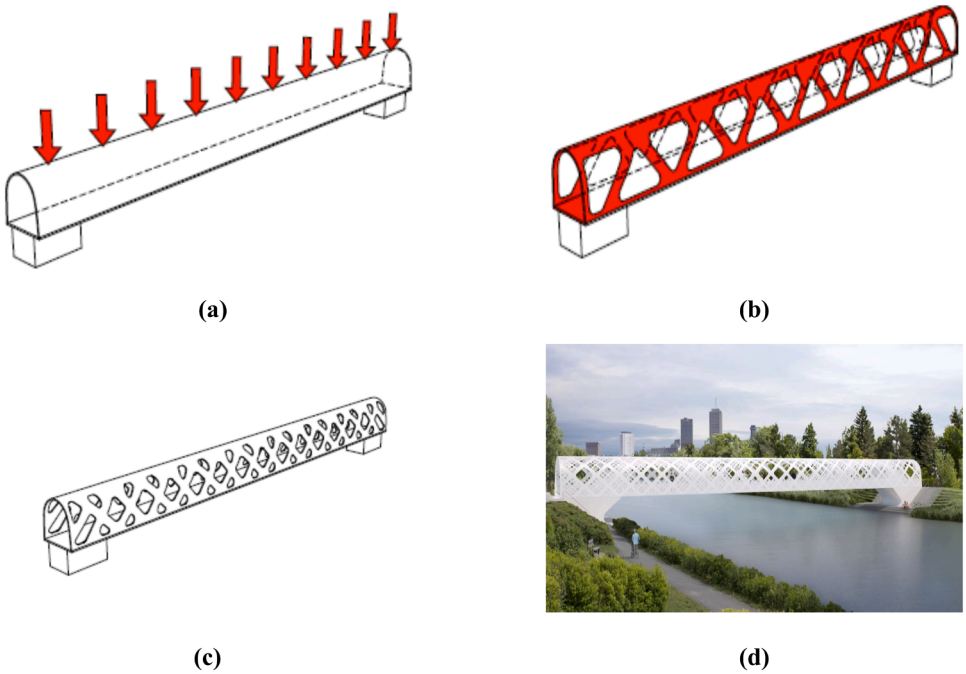

Fig. 2. Footbridge concept in Quebec City [22].

The iterative design process of the posttensioned UHPC footbridge made of precast arch elements of 5 m length is sketched in Fig. 2, which serves for architectural inspiration (for design details see [22]). By considering the distribution of the loads that the footbridge will have to resist, a first analysis identifies the unnecessary structural zones which are far from the load path. Armed with this information provided by the engineers, the architects can then control the location of the perforations throughout the bridge. This feedback loop can then be repeated as many times as necessary to achieve the balance between structural performance and architectural constraints. Based on the final design, a typical location is chosen to research. Renderings of the prototype are proposed in Fig. 3. As can be seen, because of its complex form, the prototype represents an interesting structural challenge as well as the fabrication challenge. This footbridge is combined architectural and engineering logic, all with the aim of developing a structure that would be elegant, integrated, high-performance and lightweight. From a structural perspective, the need of steel reinforcement is limited to the minimum volume possible [24]. Fig. 3-a shows the NLFEA results carried out by Sorelli et al. [22] in which a critical tensile stress of 5 MPa is estimated in the X-connection upon the application of the life load. It is then critical to assure that the UHPFRC strength is greater in such X-connections. Fig. 3-b shows the key detail of this project which is the X-connection of the latticework prefabricated element.

The objective of this study is to investigate the influence of fiber distribution on the mechanical behavior of UHPFRC X-connections, a key structural element in the complex lattice design of an original footbridge project. In addition, this study explores an innovative concept of recyclable formwork, previously utilized for acoustic UHPFRC panels [25]. Using reusable wax formwork milled by CNC enabled the production of non-standard concrete shapes without material losses, casting UHPFRC. Fiber distribution was then assessed through non-destructive testing (MIM) and image analysis of cracked sections from post-mortem specimens tested under four-point bending. Finally, a nonlinear finite element analysis (NLFEA) implementing MIM measurements, as introduced in a previous work [19], evaluated the impact of fiber distribution on the load-bearing capacity of the X-connection which was experimentally tested under bending.

This study is distinctive in its focus on fiber distribution at the element level, featuring a case study that integrates fiber distribution measurements with finite element analysis in complex-shaped UHPFRC structures, moving beyond previous research that primarily addressed rectangular beam behavior and conventional reinforcement configurations.

2. Materials and methods

2.1. UHPFRC mix design and batching protocol

In this study we employed a UHPFRC premix which is commercially available under the name of Ductal JS1000 by Lafarge-Holcim. The UHPFRC proportions consists of 2195 kg/m^3 of premix, 30 kg/m^3 of superplasticizer Fluid Premia 150 by Chryso®, 78 kg/m^3 of steel fibers (with a fiber volume fraction of 1 %), and 118 kg/m^3 of water. The premix is a proprietary mix design that incorporates an optimal combination of cement, silica fume, fine sand, and supplementary cementitious materials or fillers, all formulated to achieve an optimized packing density [26,27].

The straight steel fiber has circular cross sections with a diameter of 0.2 mm, a length of 13 mm and a tensile strength of 2860 MPa. The incorporation of 1 % steel microfibers by volume represents approximately 170 % of the raw material cost and contributes 30 % of the embodied carbon in the UHPC matrix (excluding fiber content) [28]. Due to the high cost and embodied carbon associated with steel microfibers, the fiber content was capped at 1 %, which is lower than the 2 % used in a similar study on the lattice triangle elements in the roof of the Stade Jean Bouin in Paris [2]. Consequently, this study investigates the feasibility of utilizing a lower fiber content, given that the X-connection shape and thin thickness may facilitate preferential fiber alignment and maintain adequate ductility. Ensuring the ductility of the X-connections is essential for enabling load redistribution within the statically determined lattice structure.

All mixes were prepared using a 6-liter Hobart mixer. The mixing process began with a 5-minute dry mix, after which water was added, followed by 1 minute of mixing at low speed before introducing the superplasticizer. The mix was then continued at low speed for an additional 10 minutes, followed by 5 minutes at medium speed. Steel fibers were gradually added over 2 minutes once the

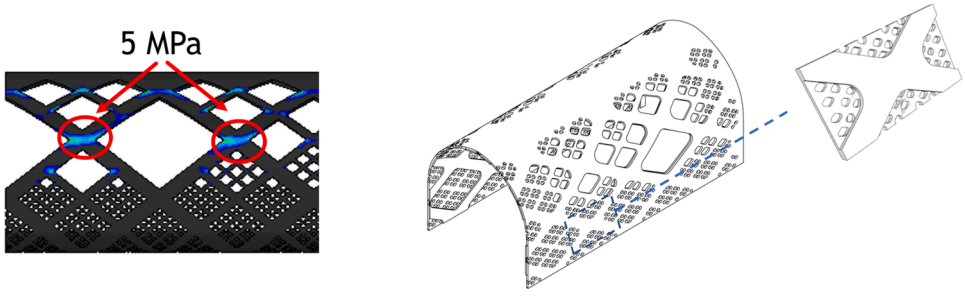

Fig. 3. (a) NLFEA analysis of the footbridge with concentration of stress in the X-connection after the application of uniform live and permanent load [22];(b)X-connection of the UHPC footbridge module.

mixture reached full workability, followed by an additional 2–3 minutes of mixing to ensure proper fiber distribution. The UHPFRC was then ready for casting. After casting, the specimens were covered with a plastic sheet and unmolded after 24 hours. All specimens underwent a curing process at 22°C and 100 % humidity for the next 28 days. After 28 days of wet curing, the UHPFRC exhibited the following characteristics: (i) a compressive strength of 140 MPa, measured in accordance with ASTM C469/C469M; (ii) a Young's modulus of approximately 50.5 GPa in compression; (iii) a load-deflection curve obtained from flexural tests conducted on three beams with dimensions of 500 mm × 100 mm × 30 mm; (iv) tensile strength determined individually from load-deflection data using inverse analysis as specified in SIA 2052 [18].

To attempt to achieve uniform fiber dispersion in the UHPFRC mixture, the process began with an initial dry mix, followed by the gradual addition of water and superplasticizer to maintain consistent workability. The fibers were then added slowly to encourage even distribution, followed by extended mixing to ensure thorough dispersion.

2.2. *Wax formwork fabrication by Computerized Numerical Control (CNC)*

The Rhinoceros 3D program, which utilizes NURBS (Non-Uniform Rational B-Splines), was employed for modeling the prototypes [29]. These virtual models were then processed using RhinoCAM, an application integrated with Rhino 3D, which generates G-code for digital manufacturing with a CNC machine [30]. The digital manufacturing tool used is a 3-axis K2 CNC milling machine (Fig. 4-b), capable of cutting within a volume of 1500 × 500 x 200 mm. It features both flat and round cutting tools (ball nose and flat end mill types) with a diameter of 6.35 mm, allowing cuts to a depth of up to 58 mm.

The wax used in this research, ConFormWax® (Fig. 4-a) is specifically developed for milling and serves as formwork for concrete [31], which has a density that enables it to withstand concrete pressure without deforming while remaining easy to mill. Its light color and melting point of 73–79°C allow it to resist sunlight in outdoor formwork applications. Additionally, the heat released by concrete hydration does not impact the mold, as the concrete is sufficiently rigid by that time to prevent any deformation. This wax was developed by Mainka et al. [31] of the Technical University of Brunswick (ITE) and is distributed by Tecete-Chemie. A representative prototype of the footbridge was selected for fabrication (Fig. 5-a). The wax mold is assembled by combining wax bricks with liquid wax, enabling the fabrication of a larger mold (Fig. 5-b). This method prevents the mold from breaking when the wax hardens [31]. Once the wax has cooled and hardened, the wax mold is milled using a CNC machine (Fig. 5-c). It is estimated that over 90 % of the wax material can be recovered after CNC milling. An even more efficient recovery might be achievable with setups specifically designed for wax grinding. After the casting phase, any impurities in the wax do not need to be removed before recasting, as debris settles to the bottom in the liquid wax and can be easily cleaned out. The cost savings associated with using wax for formwork could be substantial, as formwork expenses typically account for 35–60 % of the total project cost—a percentage that increases with more complex shapes [32]. Two formwork shapes were designed to assess the effect of the X-shape on fiber distribution during gravitational casting. The crossing angle of the X-shape was reduced by 15 %, changing from series S1x (60°) to series S2x (52°), as shown in Fig. 5-b, while keeping the other dimensions, length, width, and height, all unchanged.

2.3. *Filling the recyclable wax molds with fresh UHPFRC by gravity method*

The prototype was cast in a single step by introducing the fresh UHPFRC mixture into two hoppers located at the top corners (see Fig. 6.b), allowing fresh concrete to flow naturally under gravitational forces, without any vibration, to replicate typical manufacturing processes used for similar structural elements (Fig. 6). The reinforced wood and plastic cover were removed 24 hours after casting. The wax formwork and UHPFRC prototype were then soaked in warm water (40–50°C) for 15 minutes to soften the wax, allowing for easy separation (Fig. 7). The prototypes were subsequently kept under moist curing conditions for 28 days, then stored in the laboratory until testing. Annex 1 presents all X-shaped connections cast for series S1x and S2x, each with varying X-crossing angles. Casting was carried out without vibration to prevent fiber segregation and minimize clustering. However, specimens S11 and S12 were subjected to mechanical vibration using an external needle vibrator for two minutes immediately after casting, while all other specimens remained non-vibrated.

(a) **(b)**

Fig. 4. (a) ConFormWax®; (b) CNC milling machine.

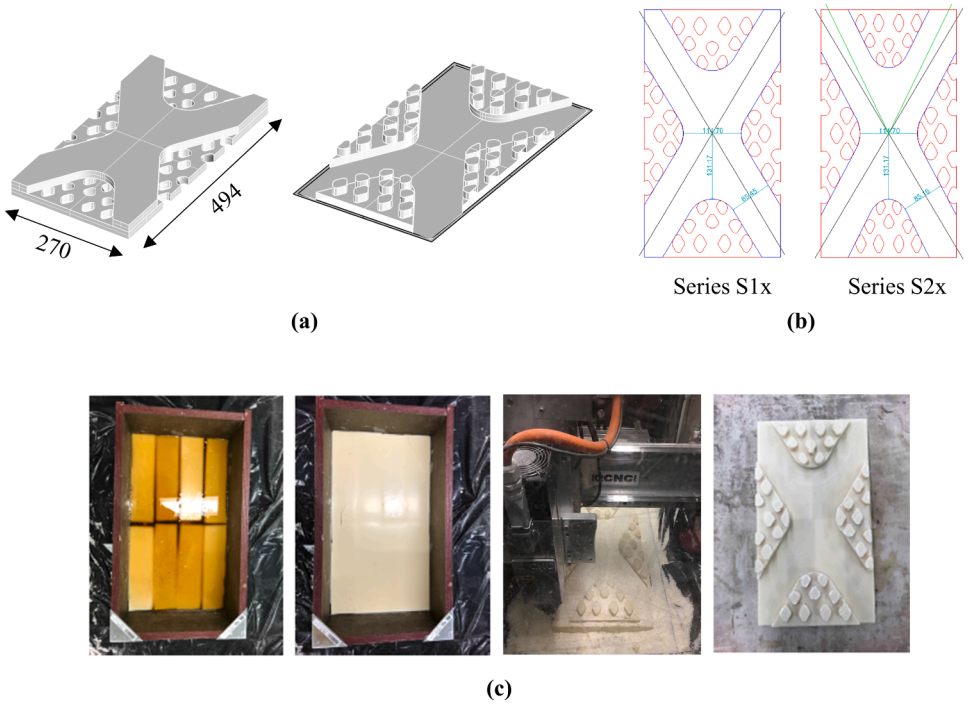

Fig. 5. (a) prototype element by Rhino and prototype mold by Rhino (b) X-connection series S1x and series S2x with different X crossing angle (c) procedure fabrication wax mold (units in mm).

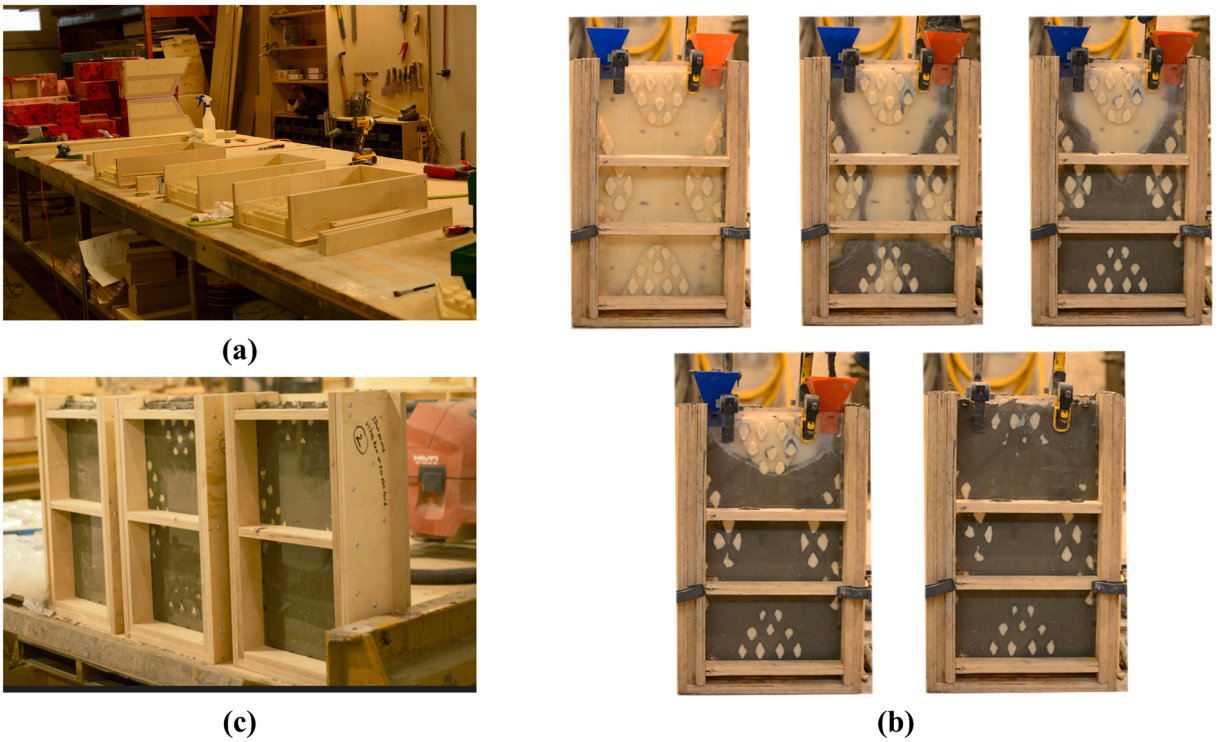

Fig. 6. (a) reinforced mold with wood (b) casting flow (c) after casting.

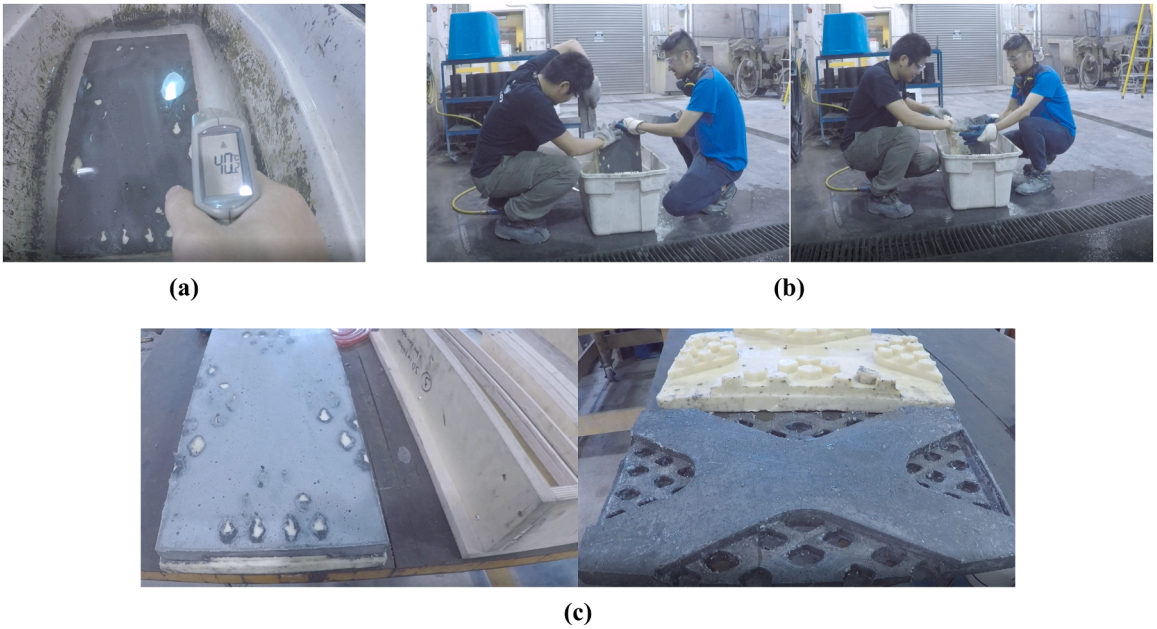

Fig. 7. Recycling the wax mold involves: (a) Soaking the prototype in warm water for 15 minutes, (b) Separating the mold and the prototype, (c) Procedures before and after demolding.

2.4. Bending tests on X-shaped connection prototype

The bending test was conducted on a 500 kN servo-hydraulic testing machine. Two Linear Variable Differential Transformers (LVDTs), positioned at one-third of the span, and a sensor located at mid-span to measure crack opening, were used to record deflection and crack opening. Additionally, Digital Image Correlation (DIC) with two digital cameras was utilized to monitor and quantify the fracture process of UHPFRC during the test (Fig. 8).

With the DIC technique, full-field strains and the fracture process were monitored throughout the test. Two Huawei P30 Pro digital cameras were positioned 150 mm from the specimen, parallel to it and aligned with the horizontal plane. The observation area targeted was a 150 mm × 80 mm region on the sheathed surface of the left and right central parts of the specimen. These cameras were used to monitor the occurrence of the first crack and its subsequent development for qualitative analysis. Prior to testing, this surface was coated with matte white paint and then sprayed to create a black speckle pattern with an approximate size of 0.3 mm. In this setup, the expected accuracy of the DIC measurements was approximately 0.5 μm. Two Linear Variable Displacement Transducers (LVDTs) with a 150 mm measuring base were positioned under the central support, with a 135 mm distance between them. A sensor was also attached to both narrow sides of the specimen to measure crack opening at the center. The crack opening sensor has a measurement limit of 6 mm.

The loading test was conducted using closed-loop control by imposing an average displacement value from the two LVDTs to maintain a stable response throughout the test. The displacement rate was set to 0.5 mm/min in the pre-peak phase and increased to 1 mm/min in the post-peak phase. The recordings from the two DIC system cameras were synchronized via wired computer control at a frequency of 0.2 Hz, while data from the other sensors were recorded at 5 Hz.

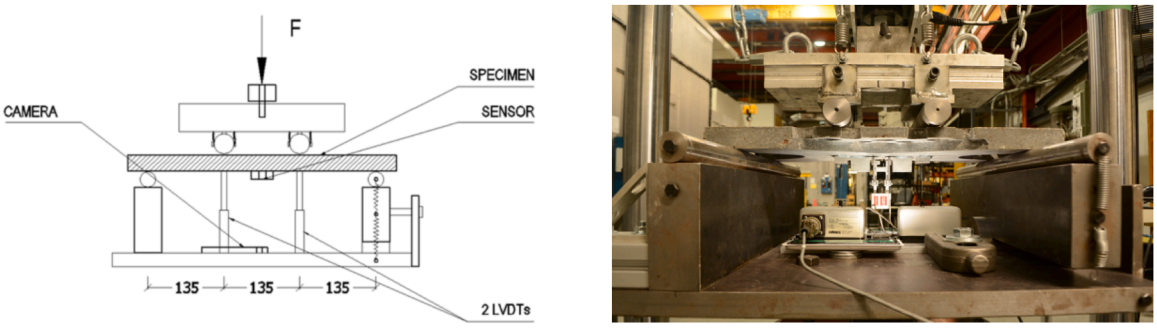

Fig. 8. Experimental setup of a bending test.

2.5. Fiber distribution measurements

2.5.1. Magnetic Inductance Methods (MIM)

A high-precision Agilent E4980A LCR Meter, set to a test frequency of 20 Hz and a signal level of 2 V (AC), was used to measure inductance with a magnetic probe [14,16,19]. Inductance measurements were performed on the panel (Fig. 9), covering both surfaces along two orthogonal directions (X and Y). Notably, the bottom surface of the specimen features the X-shaped form, while the top surface includes the hole elements (Fig. 8). The distance between each measurement point was 30 mm in both the X and Y directions, corresponding to the size of the magnetic probe. A total of 288 measurement pairs (16 rows, 9 columns, and 2 surfaces) were taken for each specimen along both orthogonal directions. The Y-direction was selected to be aligned with the main tensile force direction. The inductance measurement along two directions and, for the purpose of reference, in the air are defined as L_x, $L_y$andL_{air}, respectively. Accordingly, the relative magnetic permeability in two directions is given by $\mu_{r,X} = L_x/L_{air}$ and $\mu_{r,Y} = L_y/L_{air}$. Based on the study by Nunes et al.[14], for a specific UHPFRC mix using steel fiber, the mean relative magnetic permeability ($\mu_{r,mean}$) and fiber orientation indicator ($\rho_X - \rho_Y$), both obtained from NDT measurements on two orthogonal directions. The corresponding definitions are given by:

$$\mu_{r,mean} = \left(\mu_{r,X} + \mu_{r,Y}\right)/2 \tag{1}$$

$$(\rho_X - \rho_Y) = 0.5\frac{\mu_{r,X} - \mu_{r,Y}}{\mu_{r,mean} - 1} \tag{2}$$

$$\mu_0 = 0.57 + 1.85(\rho_X - \rho_Y) \tag{3}$$

$$\mu_1 = \begin{cases} 1.686\sqrt{\mu_0} - 0.406\mu_0 < 0.7 \\ 1\mu_0 \geq 0.7 \end{cases} \tag{4}$$

A Finite Element Model (FEM) incorporating data from the MIM measurements will be applied to predict the flexural properties of the architectural elements and will be compared with results from the four-point bending test [19]. Simultaneously, the distribution and orientation of the fibers can be assessed across two series with different geometries of architectural elements.

2.5.2. Image analysis

Following the bending test, all specimens were cut 15 mm from the localized crack, except for specimen S21, which was cut at both the localized crack and the middle position. The cut surfaces were then polished using a buffing machine and sanded with 100 and 220 μm grit sandpaper, respectively, to create a smooth finish and eliminate any distorted fiber ends from the cutting process. Chinese ink was applied to complete specimen preparation, providing a uniform surface and enhancing fiber visibility. For capturing micrographs of the UHPFRC specimens, an assembly of four 7 W lights, a Nikon camera, and a 40 mm macro lens was used. At least six micrographs were produced for each specimen. A MATLAB program was utilized to analyze specific surfaces of the UHPFRC specimens [33]. The UHPFRC micrographs were converted into binary images to facilitate the processing and initiate the analysis [34,35] (Fig. 17). White spots visible in the binary images represent UHPFRC aggregates of varying sizes. The software identifies and removes these clear aggregates by focusing only on elliptic points with diameters between 75 % and 125 % of the fiber diameter. Only white points within this specified range were considered for the computations [33]. The length of the major d_{f1} and minor axes d_{f2} of the ellipse were determined to calculate the fiber orientation. Thus, the orientation angle of each fiber is given by:

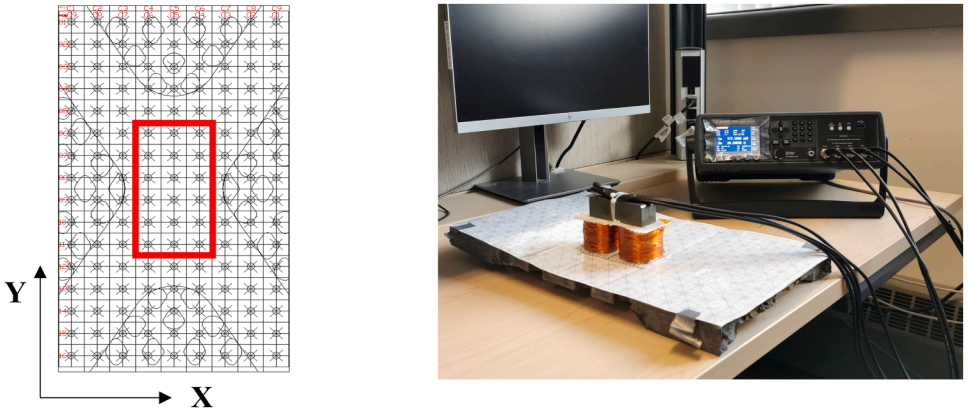

Fig. 9. Magnetic Inductance Measurement (MIM) using a magnetic probe: (a) location and direction of measurements; (b) test setup (unit: mm).

$$\theta = \cos^{-1}\left(\frac{d_{f2}}{d_{f1}}\right) \tag{5}$$

This method tends to overestimate the lower angles, a limitation noted by other authors [36,37]. As a result, the orientation angle of fibers is considered statistically valid in this study, but its accuracy is not evaluated or discussed. After counting the fiber by MATLAB program, the fiber orientation factor μ_0^{IA}, which is defined as the probability of a single fiber being intersected by a considered section, is obtained by the following equation [38,39]:

$$\mu_0^{IA} = n_f \frac{A_f}{V_f} \tag{6}$$

where n_f is the number of fibers crossing a unit area, A_f is the cross-section of a fiber.

Based on the analysis results, the total number of fibers (by Image analysis and manual counting), the number of fibers per unit area n_f, the average orientation of fiber and the fiber orientation factor μ_0^{IA} are given in Table 5. The image analysis underestimated the fiber count by approximately 3 % compared to manual counting, due to the conversion of the original image into a binary format [40].

2.6. Non-linear finite element analysis (NLFEA) coupled with MIM

A Nonlinear Finite Element Analysis (NLFEA) using Abaqus Finite Element Software was conducted to gain a better understanding of the effect of fiber distribution on the mechanical behavior of the X-connections. In detail, NLFEA was conducted to evaluate the behavior of UHPFRC X-connections under bending by considering the actual fiber distribution as measured by the Magnetic Inductance Method (MIM). The Finite Element Method (FEM) model employed in this analysis was developed and validated in previous work by Tran et al. [19]. To account for the nonlinear stress-strain behavior in both compression and tension of UHPFRC, the Concrete Damaged Plasticity (CDP) model from the commercial software Abaqus was utilized [43]. This model has been effectively applied in earlier studies to analyze the structural responses of UHPFRC structures, including bridge decks and beam bridges [41–43]. Notably, the CDP model was modified to incorporate a non-uniform tensile law that depends on the local distribution of fibers. This approach involves assigning a local tensile law at each FEM point based on the fiber parameter (λ) distribution, as quantified using the Metal Injection Molding (MIM) technique, as illustrated in Fig. 13 and Fig. 14. Comprehensive details of the model can be found in a prior publication [19]. As main limitations, the employed model is grounded in continuum mechanics and does not directly account for composite heterogeneity, unlike previous mesoscale models [44]. Moreover, its calibration will be limited to the load-deflection

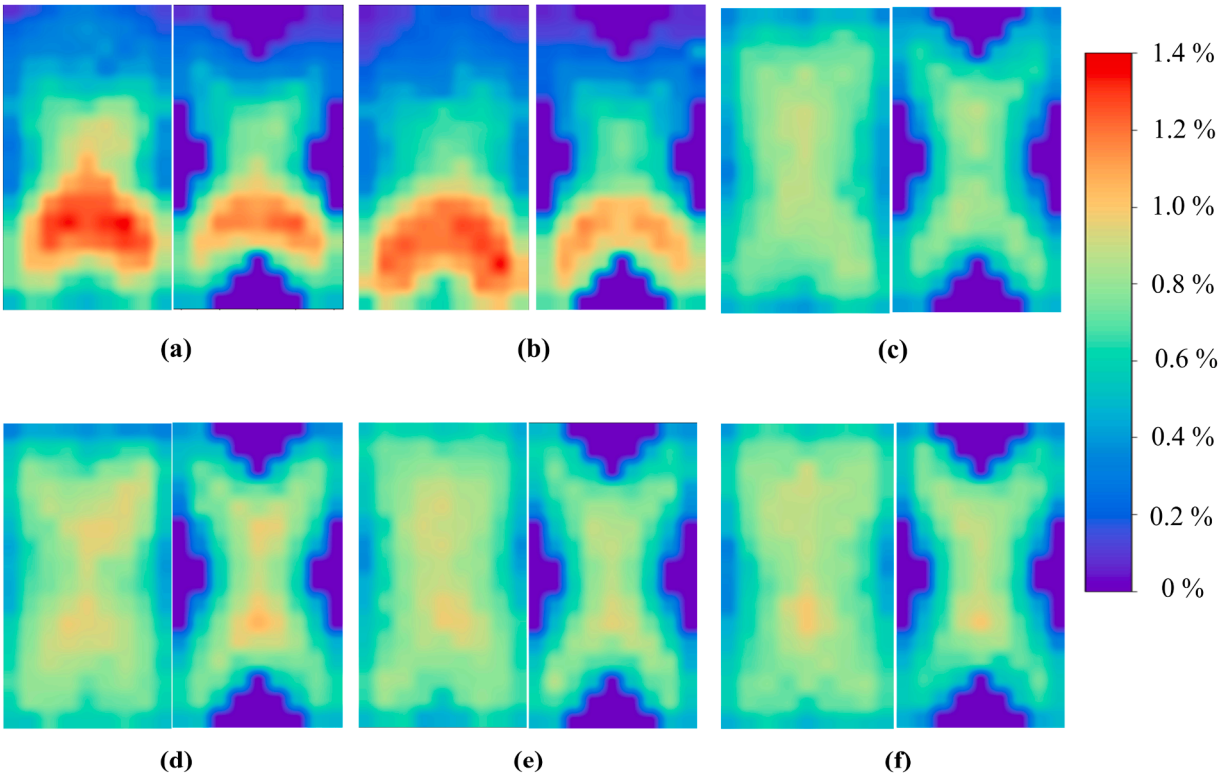

Fig. 10. Contour maps for fiber volume fraction V_f: (a) S11 top and bottom, (b) S12 top and bottom, (c) S13 top and bottom, (d) S21 top and bottom, (e) S22 top and bottom, (f) S23 top and bottom.

behavior observed in bending tests, without the integration of multiple testing methods [45].

3. Test results

3.1. Fiber distribution

Fig. 10, Fig. 11 and Fig. 12 present contour maps of the local fiber volume fraction V_f, orientation factor μ_0, and efficiency factor for each X-specimen μ_1, based on non-destructive testing (NDT) measurements on both the top and bottom surfaces. Fig. 10.a and 10.b clearly show that specimens S11 and S12 exhibit noticeable differences between the upper and lower parts. This significant fiber segregation is attributed to external vibration resulting from the 3-hour transport from the casting facility to the laboratory immediately after casting. The other specimens, S13, S21, S22, and S23, did not exhibit significant fiber segregation, as they were not exposed to vibration. Nonetheless, the X-shape induces a slight concentration of fibers within the X-connection area due to its complex geometry, a pattern that is qualitatively visible in all specimens shown in Fig. 10. provides a quantitative summary of the measured mean values (denoted with an overbar) and the coefficients of variation (CV) for each parameter, $\widehat{Cv}$ of the fiber volume (V_f) and fiber factors (μ_0,μ_1, λ) for the central area of each specimen (which is from the 6th to 11th row and from the 4th to 6th column as indicated in Fig. 22.a). The mean local volume (V_f) was approximately 0.84 % with a mean coefficient of variation (Cv) of 17 % for the vibrated specimens S11 and S12. The mean local volume (V_f) for all specimens (without vibration) was about 0.87 % with a mean Cv of 6 %. The fiber distribution parameters μ_0 andμ_1 exhibited considerable variation, with values reaching up to 31 % for specimens S1 and S2, and up to 14 % for the remaining specimens. The distribution of the dimensionless parameter $\lambda = V_f\mu_0\mu_1$ as calculated by Shen et al. [16] is also shown in Fig. 13 to serve as a reference value for the bending strength.

Additionally, Fig. 14 provides a zoomed-in view of parameter λ in the central area (from the 6th to the 11th row and from the 4th to the 6th column, as shown in Fig. 22.a). This is the zone of interest in the bending test, where stress is concentrated due to the shape. The location of the observed localized crack is also indicated.

Table 2 and Table 3 present the same values as Table 1, but specifically for the area where the crack localized after the bending test, as well as for the two rows of MIM (Magnetic Inductance Method) probed volumes across the mid-section (i.e., from the 7th to 8th row and from the 4th to 6th column, as indicated in Fig. 22.a). For all specimens, the fiber volume is lower in the zone where cracks localize, indicating a weaker area. These values will be referenced in the discussion in the following sections.

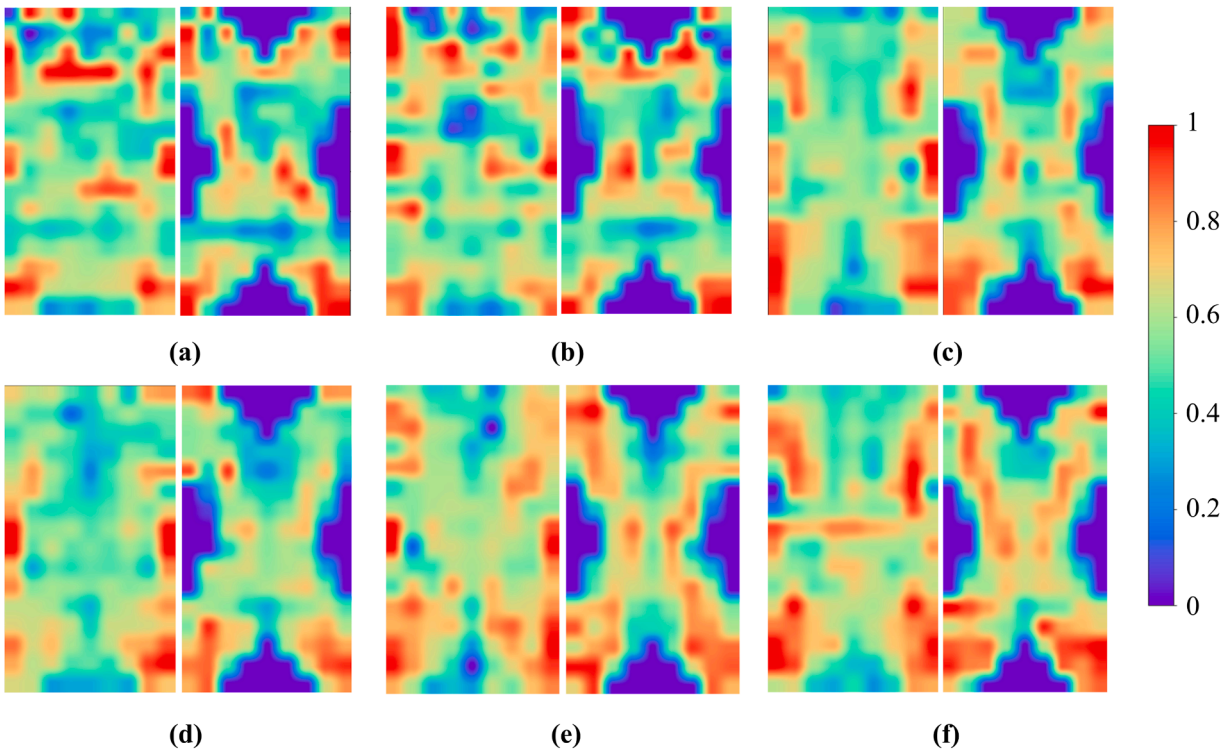

Fig. 11. Contour maps for fiber orientation factor μ_0: (a) S11 top and bottom, (b) S12 top and bottom, (c) S13 top and bottom, (d) S21 top and bottom, (e) S22 top and bottom, (f) S23 top and bottom.

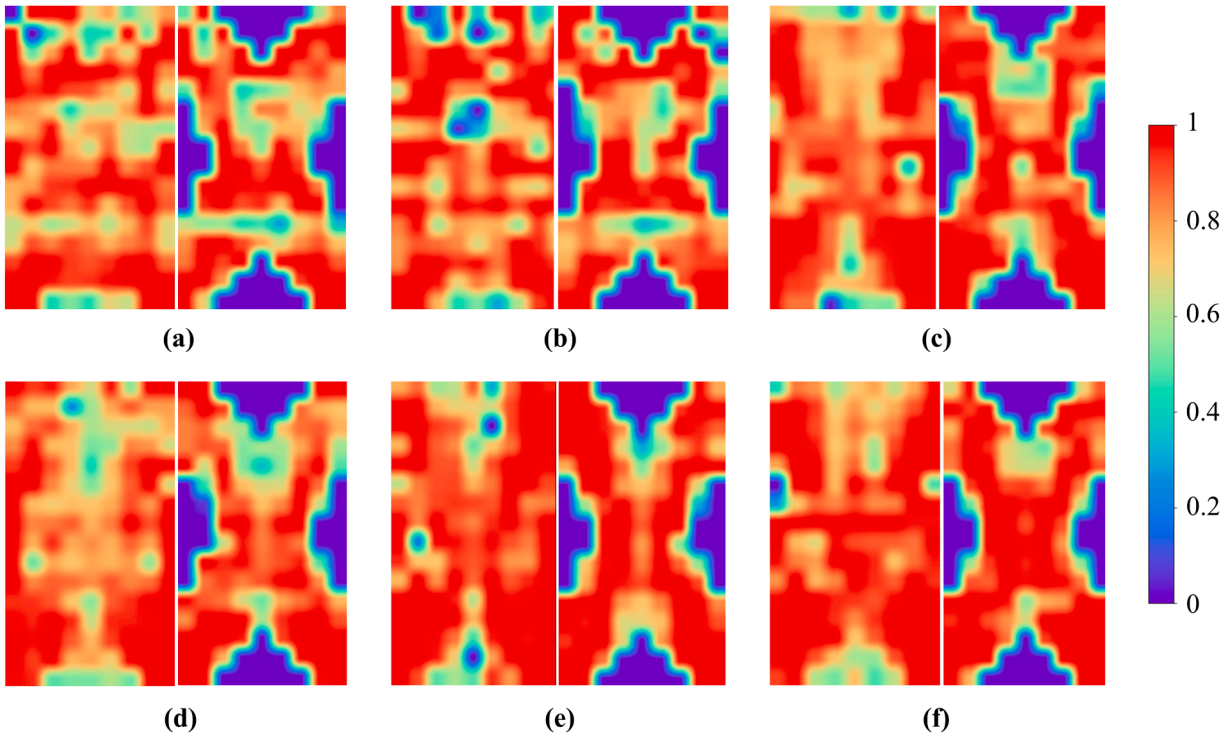

Fig. 12. Contour maps for fiber orientation factor μ_1: (a) S11 top and bottom, (b) S12 top and bottom, (c) S13 top and bottom, (d) S21 top and bottom, (e) S22 top and bottom, (f) S23 top and bottom.

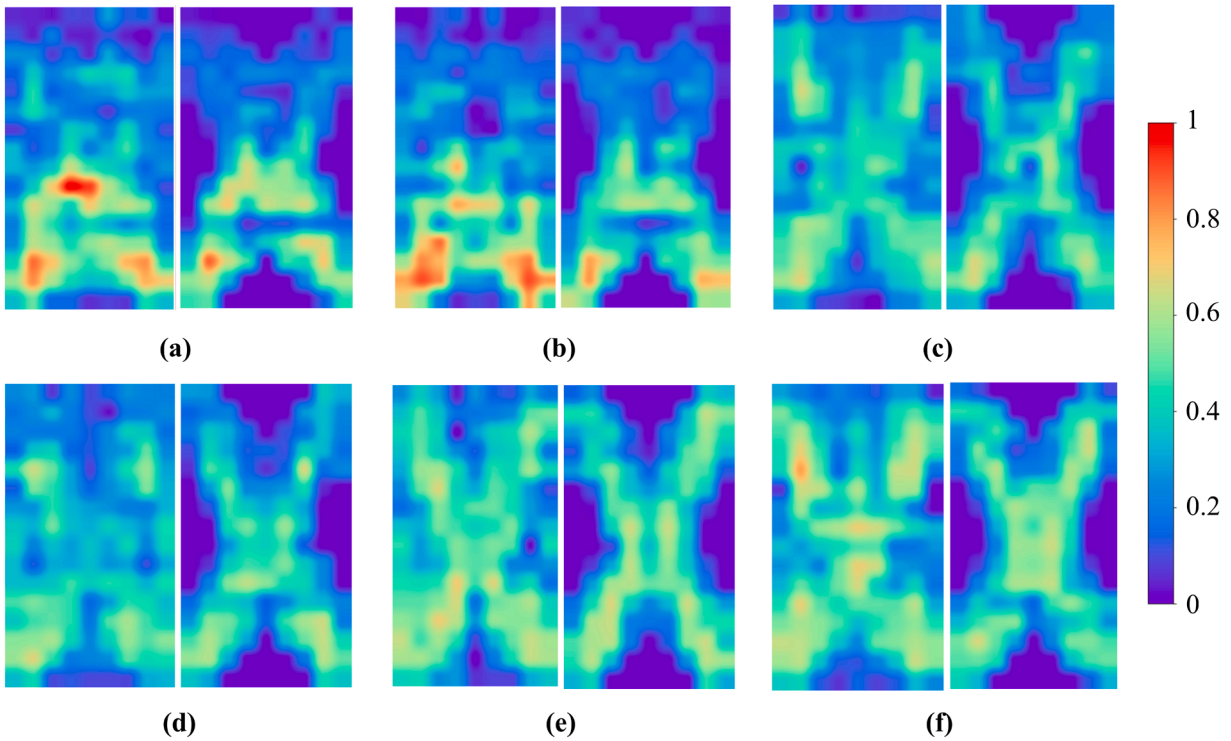

Fig. 13. Contour maps of dimensionless parameter λ: (a) S11 top and bottom, (b) S12 top and bottom, (c) S13 top and bottom, (d) S21 top and bottom, (e) S22 top and bottom, (f) S23 top and bottom.

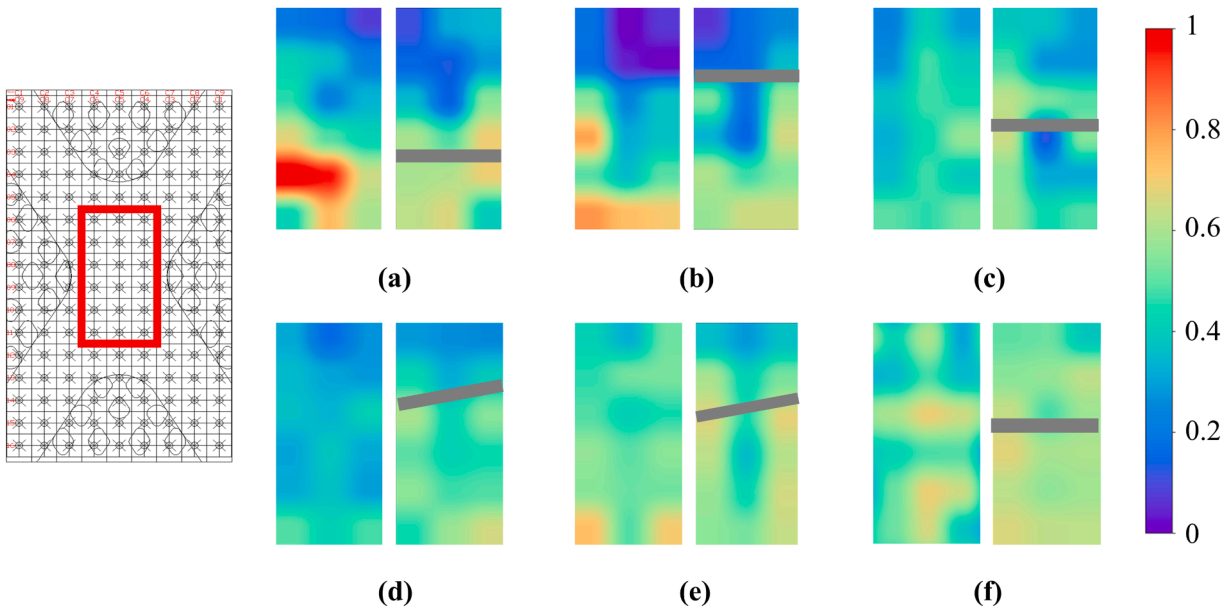

Fig. 14. Contour maps of dimensional parameter λ in the central area (squared with red line in the top left figure from 6th to 11th row and from 4th to 6th column): (a) S11 top and bottom, (b) S12 top and bottom, (c) S13 top and bottom, (d) S21 top and bottom, (e) S22 top and bottom, (f) S23 top and bottom.

3.2. Flexural response of X-connection

Although testing the X-connections under direct tension would more accurately represent their behavior in the actual structure (as shown in Fig. 3.a), this approach is highly challenging. The primary difficulties lie in precisely aligning the applied load with the central axis of the sample and in preventing damage to the gripped zones [46]. For simplicity, the X-connection specimens were tested under bending, which still provides relevant insights into how fiber distribution and stress concentration due to complex shapes can influence the cracking behavior.

3.2.1. Flexural strength-deflection responses

Figs. 15a and 15b present the bending test results, displaying flexural strength versus deflection and flexural strength versus crack opening curves at the mid-section (114.7 x 30 mm), respectively. The thick black line represents the average response. Both deflection and crack opening are shown as average values measured from the LVDTs. All specimens exhibit significant flexural-hardening behavior, with flexural strength ranging from 17.5 to 34.2 MPa at the mid-section (114.7 x 30 mm). Similar flexural strength values for UHPFRC with 1 % fiber content have been reported in other studies [47,48]. The variation of flexural strength can be explained by the variation of local fiber distribution within the specimen (Table 1) and is discussed in the next section.

The lowest strength of specimen S12 can be explained by its low fiber volume fraction of 0.77 % and the high dispersion values (Table 2 and Fig. 14). This means an uneven distribution, with the weakest zone located in the midspan section, where the first crack is likely to form, making it less likely for multiple cracks to develop in the surrounding areas. Similar outcomes are observed when comparing values in the localized crack (Table 2) and in the mid-span area (Table 3, from the 8th to 9th row and from the 4th to 6th column), where low fiber volume and high dispersion contribute to reduced strength. The superior strength of specimen S21 can be attributed to the high level of uniformity (i.e., low coefficient of variation) in fiber volume (V_f=0.9 %) and fiber orientation parameters μ_0 and μ_1 (Table 2). Despite their low absolute values, this uniformity delays crack localization, confirming the importance of uniform fiber distribution in areas of stress concentration. As found in previous work the more the fibers and multiple cracks are uniform, the more the response is ductile [16,19]. The uniformity of the λ parameter for specimen S21 is also evident in Fig. 14.

3.2.2. Crack patterns by DIC analysis

The fracture process of all specimens was assessed using Digital Image Correlation (DIC) analysis with the open-source Ufreckles software, developed by Réthoré [49]. Fig. 16 shows three graphs of representative fracture processes from six specimens S11, S12, S13, S21, S22 and S23, respectively. In each graph, point A′ refers to the moment when the first crack is detected based on DIC analysis, point B′ corresponds to the peak-load point, and point C′ is an arbitrary point on the softening branch after crack localization. Instead of forming numerous micro-cracks before reaching localization, only 2–9 macro-cracks, clearly visible to the naked eye, developed after the experiment. Notably, the typical multiple-crack behavior seen in thin UHPC panels was significantly reduced due to the stress concentration in the X-connection. Thus, the X-connection restricts the formation of multiple micro-cracks and promotes the localization of stress in larger cracks.

Table 1
Mean values and standard deviation of the fiber distribution parameters V_f, μ_0, μ_1 and λ in central area (i.e., in Fig. 9.a from 6th to 11th row and from 4th to 6th column).

	S11			S12			S13			S21			S22			S23		
	Top	Bottom	Both	Top	Bottom	Both	Top	Bottom	Both	Top	Bottom	Both	Top	Bottom	Both	Top	Bottom	Both
$\overline{V_f}$(%)	0.98	0.85	0.91	0.80	0.75	0.77	0.86	0.79	0.82	0.90	0.90	0.90	0.90	0.86	0.88	0.87	0.86	0.87
$\widehat{Cv}$	18 %	15 %	17 %	19 %	15 %	17 %	3 %	6 %	5 %	6 %	8 %	7 %	4 %	5 %	5 %	6 %	6 %	6 %
$\overline{\mu_0}$	0.55	0.57	0.56	0.50	0.58	0.54	0.56	0.60	0.58	0.49	0.58	0.53	0.62	0.66	0.64	0.65	0.69	0.67
$\widehat{Cv}$	17 %	18 %	17 %	23 %	20 %	21 %	7 %	14 %	11 %	7 %	10 %	8 %	7 %	13 %	10 %	10 %	7 %	9 %
$\overline{\mu_1}$	0.80	0.83	0.82	0.73	0.83	0.78	0.85	0.87	0.86	0.77	0.86	0.82	0.91	0.92	0.92	0.93	0.97	0.95
$\widehat{Cv}$	15 %	17 %	16 %	31 %	18 %	25 %	8 %	13 %	11 %	8 %	10 %	9 %	6 %	9 %	8 %	8 %	4 %	6 %
$\overline{\lambda}$	0.47	0.43	0.45	0.37	0.39	0.38	0.41	0.43	0.42	0.34	0.45	0.40	0.51	0.52	0.52	0.54	0.58	0.56
$\widehat{Cv}$	26 %	21 %	24 %	27 %	21 %	24 %	9 %	14 %	12 %	8 %	12 %	10 %	9 %	13 %	11 %	13 %	7 %	10 %

Table 2
Mean values and standard deviation of the fiber distribution parameters V_f, μ_0, μ_1 and λ around the localized crack.

	S11			S12			S13			S21			S22			S23		
	Top	Bottom	Both	Top	Bottom	Both	Top	Bottom	Both	Top	Bottom	Both	Top	Bottom	Both	Top	Bottom	Both
$\overline{V_f}$(%)	0.95	0.81	0.88	0.70	0.70	0.70	0.84	0.75	0.80	0.91	0.89	0.90	0.86	0.80	0.83	0.84	0.82	0.83
$\widehat{Cv}$	11 %	10 %	10 %	4 %	5 %	5 %	4 %	5 %	5 %	6 %	7 %	7 %	4 %	6 %	5 %	5 %	5 %	5 %
$\overline{\mu_0}$	0.62	0.77	0.70	0.62	0.67	0.65	0.59	0.68	0.63	0.46	0.53	0.50	0.59	0.78	0.69	0.72	0.74	0.73
$\widehat{Cv}$	12 %	18 %	15 %	16 %	26 %	21 %	6 %	20 %	13 %	2 %	7 %	4 %	4 %	17 %	11 %	11 %	9 %	10 %
$\overline{\mu_1}$	0.89	0.96	0.93	0.89	0.89	0.89	0.89	0.91	0.90	0.74	0.82	0.78	0.89	0.96	0.93	0.96	0.98	0.97
$\widehat{Cv}$	9 %	6 %	8 %	14 %	14 %	14 %	14 %	19 %	16 %	3 %	8 %	5 %	5 %	7 %	6 %	5 %	4 %	4 %
$\overline{\lambda}$	0.53	0.59	0.56	0.87	0.43	0.65	0.44	0.49	0.47	0.31	0.38	0.35	0.45	0.60	0.53	0.58	0.60	0.59
$\widehat{Cv}$	13 %	11 %	12 %	22 %	22 %	22 %	8 %	19 %	14 %	4 %	6 %	5 %	4 %	13 %	8 %	11 %	7 %	9 %

Table 3
Mean values and standard deviation of the fiber distribution parameters V_f, μ_0, μ_1 and λ in the narrow central area (i.e., in Fig. 9.a from 7th to 8th row and from 4th to 6th column).

	S11			S12			S13			S21			S22			S23		
	Top	Bottom	Both	Top	Bottom	Both	Top	Bottom	Both	Top	Bottom	Both	Top	Bottom	Both	Top	Bottom	Both
$\overline{V_f}$(%)	0.94	0.78	0.86	0.73	0.69	0.71	0.84	0.75	0.80	0.84	0.83	0.84	0.87	0.81	0.84	0.84	0.82	0.83
$\widehat{Cv}$	7 %	7 %	7 %	8 %	4 %	6 %	4 %	5 %	5 %	5 %	5 %	5 %	3 %	5 %	4 %	5 %	5 %	5 %
$\overline{\mu_0}$	0.55	0.66	0.60	0.65	0.66	0.65	0.59	0.68	0.63	0.52	0.64	0.58	0.62	0.74	0.68	0.72	0.74	0.73
$\widehat{Cv}$	12 %	22 %	17 %	17 %	26 %	21 %	6 %	20 %	13 %	4 %	8 %	6 %	5 %	16 %	10 %	11 %	9 %	10 %
$\overline{\mu_1}$	0.83	0.88	0.86	0.90	0.90	0.90	0.90	0.91	0.90	0.81	0.93	0.87	0.92	0.95	0.93	0.96	0.98	0.97
$\widehat{Cv}$	12 %	17 %	15 %	11 %	11 %	11 %	11 %	19 %	15 %	5 %	7 %	6 %	5 %	9 %	7 %	5 %	4 %	4 %
$\overline{\lambda}$	0.44	0.47	0.45	0.85	0.40	0.63	0.44	0.49	0.47	0.35	0.49	0.42	0.50	0.57	0.53	0.58	0.60	0.59
$\widehat{Cv}$	15 %	20 %	17 %	19 %	22 %	20 %	8 %	19 %	14 %	4 %	7 %	6 %	6 %	13 %	10 %	11 %	7 %	9 %

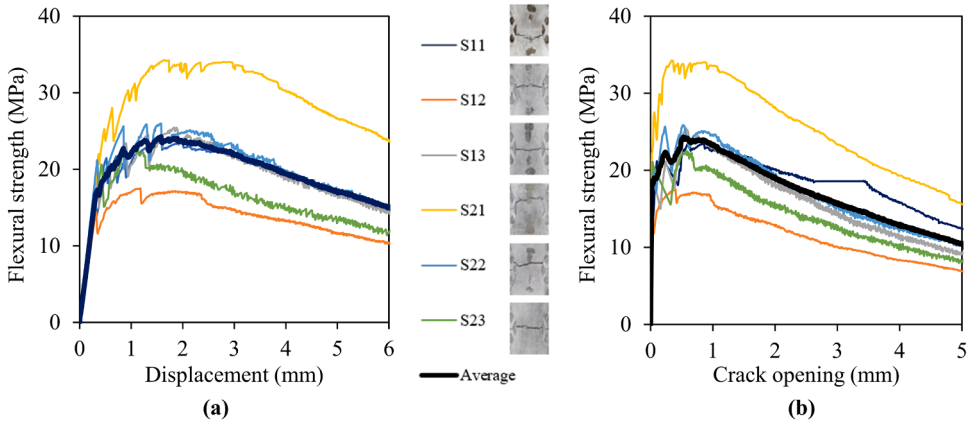

Fig. 15. (a) Flexural strength – deflection response of 6 specimens at middle section (110x30mm); (b) Flexural strength – crack opening curve of 6 specimens at middle section (110x30mm).

Specimen S21 displayed the highest number of micro-cracks and also showed the greatest flexural strength. In contrast, specimen S23 showed the highest λ in the central zone, but its flexural strength was lower than that of specimens S21, S22, and S13. This can be attributed to the fracture process: a single crack formed in the center of the central area, where localized stress concentration ultimately led to collapse. This failure was preceded by only a few microcracks, as illustrated in Fig. 16.f.

Table 4 summarizes the number of cracks on each specimen. Except for specimen S21, the strain-hardening local response was recorded before locating the fictitious crack (Fig. 16-d). More specifically, the first crack of this specimen did not appear in the central region. It can be concluded that localized deficiencies in fiber distribution beyond this area are the primary contributing factors. This leads to cracks forming in the larger cross-sectional area and shows the advantage of UHPFRC although it has the smallest λ in the center. The specimen displaying the highest number of multiple microcracks S21 also exhibited the highest flexural strength. On the contrary, specimen S23 with the highest λ in the center zone exhibited a lower flexural strength than those of the specimens S21, S22 and S13. The reason can be explained by the fracture process: a crack occurred in the middle of the central area forming the collapse mechanism with formation of very few micro-cracks in the neighborhood zones (Fig. 16-f).

3.2.3. Image analysis of fiber distribution

Fiber distribution plays an important role in the structural behavior of such X-connection. Table 5 presents the summary of fiber counting and the average orientation. As anticipated, the weakness of specimen S12 can be attributed to its low fiber count, minimal fiber density per unit area, and the fiber orientation factor μ_0^{IA}. Specimen S21 exhibits the highest fiber density per unit area across both cutting plane configurations. In contrast, the parameters in the other specimens (S11, S13, S22, and S23) show no significant differences. This confirms the correlation between fiber density per unit area n_f and the flexural strength of the specimens.

A discrepancy of 5–47 % exists between the fiber orientation factor and values obtained through the Magnetic Inductance Method (MIM), which can be attributed to the influence of edge effects and the presence of narrow sections with holes on the magnetic measurements. In fact, only in the central area does the cross-sectional width (114.7 mm) exceed the probed size of the Magnetic Inductance Method (MIM), which is approximately 100 mm. Consequently, MIM measurements at the 4th and 6th columns (Fig. 22.a) are influenced by edge effects, as the probe ends extend partially beyond the concrete surface. For example, Fig. 18 highlights a black area with low fiber content near the localized crack in specimen S21 that was detected. This area contributed to a longitudinal crack in the specimen, as measured by DIC (Fig. 16-d). The relatively even fiber distribution in specimen S21 (Fig. 14.d) explains its fracture process, with the first crack forming away from the middle section in a weak area, subsequently followed by multiple additional cracks.

3.2.4. Image analysis of fiber distribution

Table 5 presents a summary of fiber counting and the average orientation μ_0^{IA}, as measured by image analysis on the cracked section of the post-mortem specimen. For the sake of comparison the fiber orientation factor and the μ_0^{MIM} is also reported.

The low flexural strength of specimen S12 can be attributed to its minimal fiber count, low fiber density per unit area, and fiber orientation factor μ_0^{IA}. In contrast, specimen S21 demonstrated the highest fiber density per unit area, observed in both the cutting plane near the localized crack and the midspan section.

It is important to note a mismatch ranging from 5 % to 47 % between the fiber orientation factor μ_0^{IA} and the values μ_0^{MIM} measured by the Magnetic Inductance Method (MIM). This discrepancy suggests that the MIM may not be ideally suited for measuring thin UHPFRC slab with holes. While the probe head measures about 30 mm, the full probe size is approximately 100 mm, and only in the central area does the cross-sectional width (114.7 mm) exceed this size. As a result, MIM measurements at the 4th and 6th columns are affected by edge effects, as the probe ends partially extend beyond the concrete surface.

Fig. 18 shows a black area with low fiber content near the localized crack in specimen S21, which likely caused a longitudinal crack in the specimen, as measured by the Digital Image Correlation (DIC) in Fig. 16-d. The relatively even fiber distribution in specimen S21

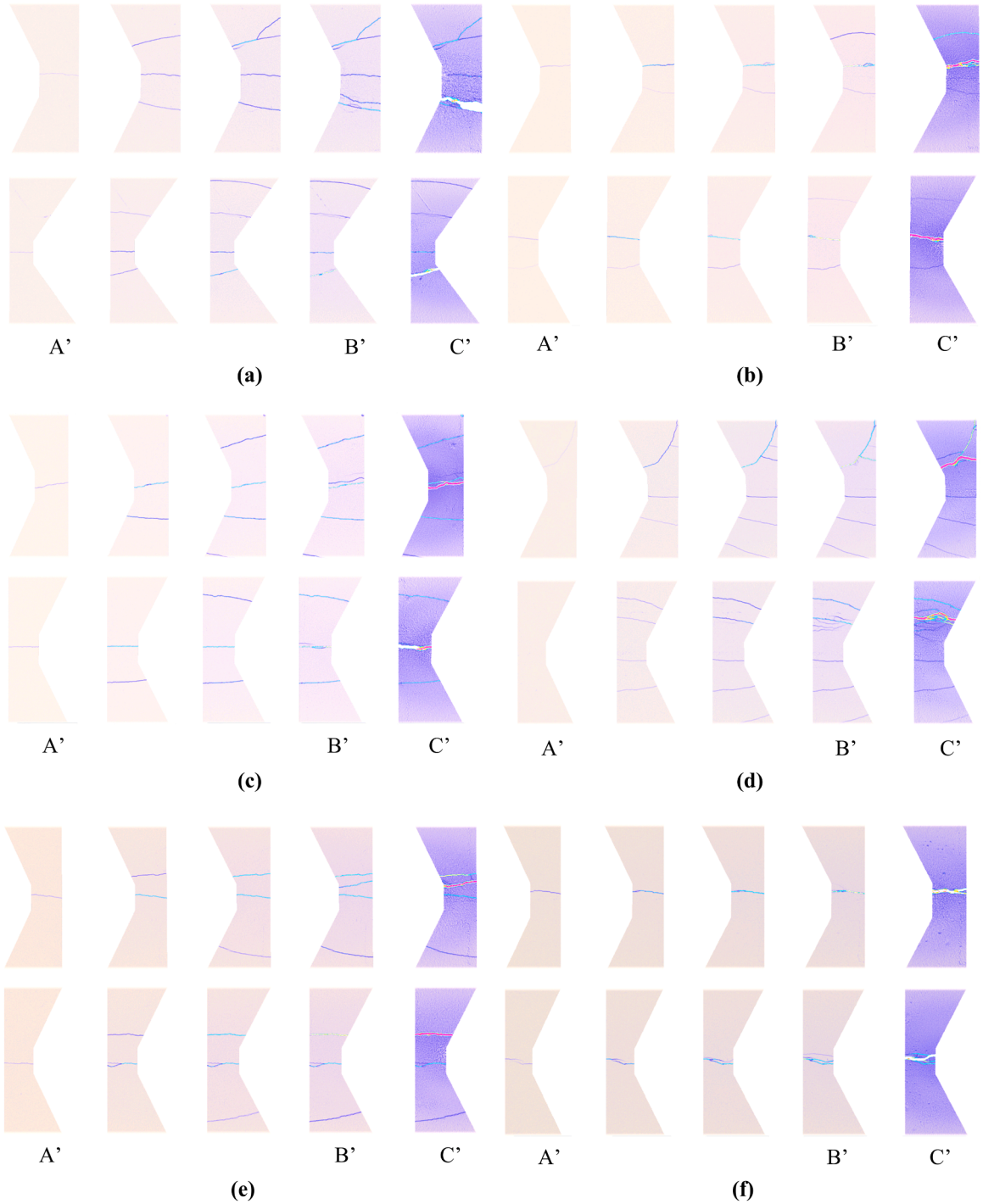

Fig. 16. Fracture processes of specimen (a) S11; (b) S12; (c) S13; (d) S21; (e) S22; (f) S23.

Table 4
Number of cracks detected by DIC.

Specimen	S11	S12	S13	S21	S22	S23
Number of cracks	4	3	5	9	4	2

Table 5
Summary of fiber counting and orientation.

Specimen	S11	S12	S13	S21	S22	S23
N^0 of fiber by image analysis	702	489	826	1207	846	693
N^0 of fiber manual counting	725	507	830	1225	852	694
Fiber/mm^2	0.20	0.14	0.21	0.27	0.18	0.19
Average orientation (°)	48	43	44	50	45	45
μ_o^{IA}	0.62	0.44	0.66	0.84	0.57	0.60
μ_o^{MIM}	0.70	0.65	0.63	0.5	0.69	0.73

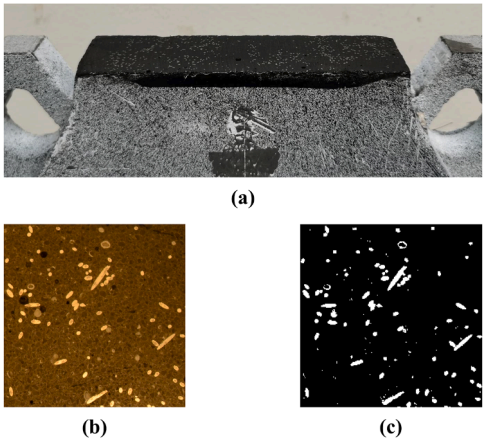

Fig. 17. (a) Specimen after cutting, polishing, and painting; Example of input and output images by MATLAB program (b) original image; (c) binary image.

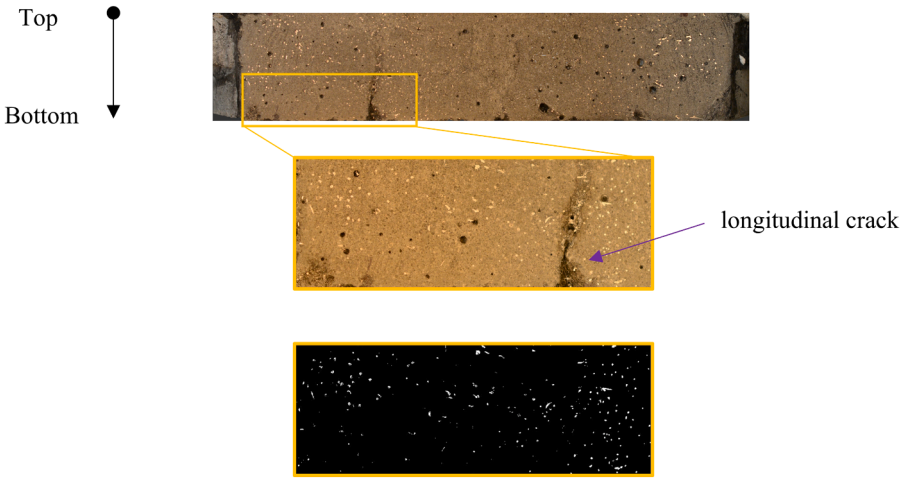

Fig. 18. Example of uneven fiber distribution at the section near the localized crack of specimen S21.

(Fig. 14.d) accounts for the observed fracture process, with the first crack forming away from the middle section (Fig. 16.d) where fiber density per unit area is higher (Table 5).

3.2.5. Correlation study

This section aims to study possible correlation between fiber distribution and flexural performances of the X-specimens. Fig. 19 illustrates the correlation between various variables, such as maximum moment M_{max}, energy dissipated W* (in Table 7) and the number of fibers intercepting the localized crack, the orientation factor$\mu_o^{IA}$from the Eq. (6) and image analysis, the orientation factor μ_o^{MIM} from MIM, and the number of cracks detected by DIC. The high coefficients of determination (R^2) confirm the linear relationship between the maximum moment (M_{max}), the effective crack width (W^*), and the number of fibers intercepting the localized crack. That

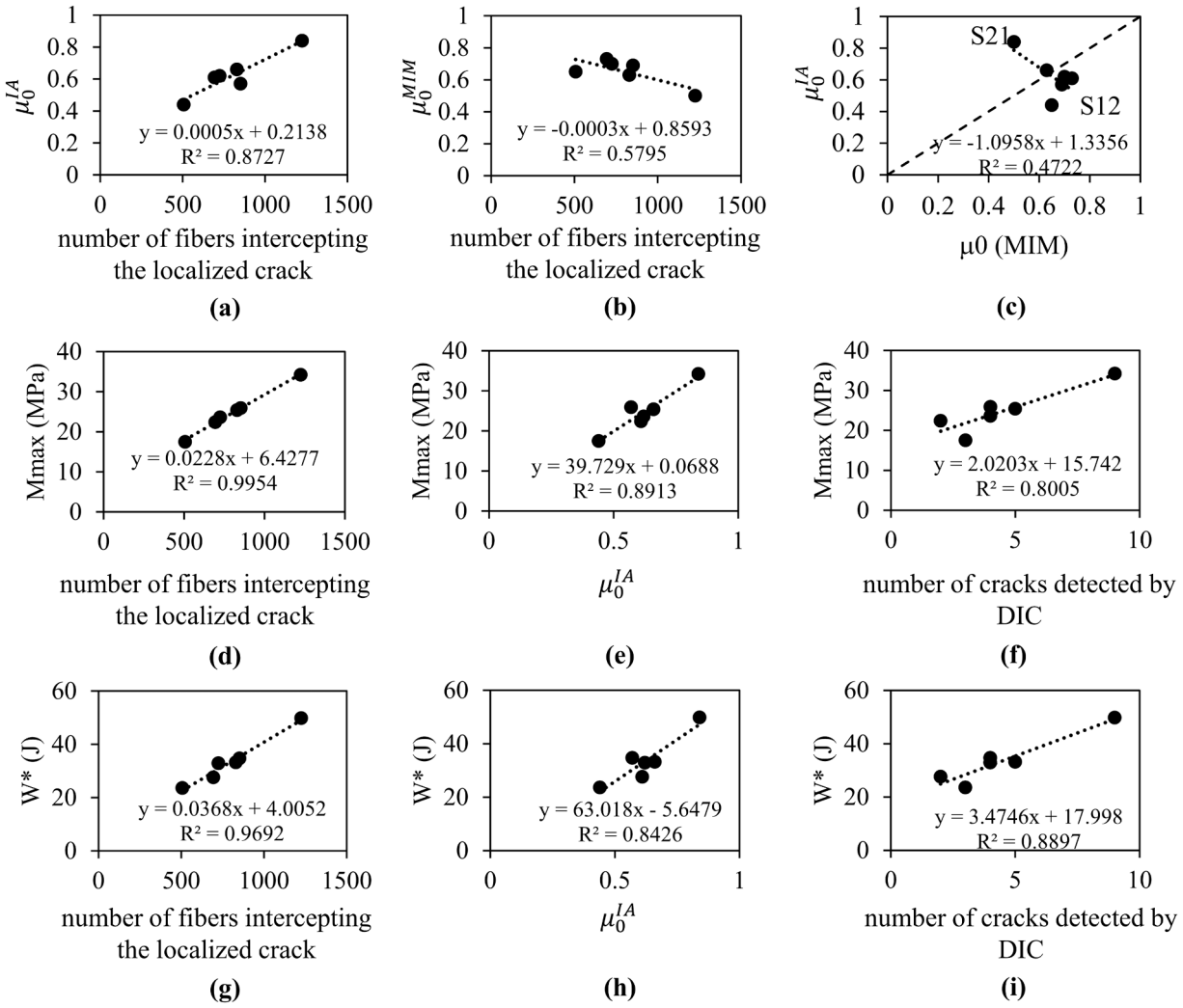

Fig. 19. Correlation study between (a)μ_0^{IA}– number of fibers intercepting the localized crack; (b) μ_0^{MIM}– number of fibers intercepting the localized crack; (c)μ_0^{IA}– μ_0^{MIM}; (d) M_{max} – number of fibers intercepting the localized crack; (e) M_{max} – μ_0^{IA}; (f) M_{max} – number of cracks detected by DIC; (g) W* – number of fibers intercepting the localized crack; (h) W* – μ_0^{IA}; (i) W* – number of cracks detected by DIC;.

is, the number of fibers distributed in the middle section of the X-connection is a critical factor for the element strength. Other quantities, such as μ_o^{IA} and the number of cracks from the DIC, also show a satisfactory correlation. However, as shown in Fig. 19-c, the orientation factor μ_0^{MIM} estimated by MIM does not well correlate with the μ_0^{IA}especially for the 2 specimens S12, S21. This highlights the limitations of applying MIM techniques to complex-shaped UHPC elements, due to potential edge effects impacting the instrument's reference volume probe.

3.2.6. Discussion on the effect of the X-angle and the position of the localized crack

Fig. 20 illustrates the effect of inclination angle and vibration on flexural strength and the number of fibers intersecting the localized crack, as measured through image analysis. The mean values for specimens S11 and S12, influenced by mechanical vibration, affect both the flexural strength and the number of fibers bridging the localized crack. The comparison between specimen S13 and the mean values of S2 specimens (S21, S22, S23) reveals similar results in terms of flexural strength and the number of fibers bridging the localized crack. This indicates that altering the cross-angle of X-connection from 60° to 52° had only a minimal effect on fiber distribution.

Fig. 21 displays the location of the localized crack observed at the conclusion of the bending test. As anticipated, due to stress concentration at the X-shaped connections, all cracks are confined to the central region, between the two mounts of the sensor that measures crack opening. Specimens S13 and S23, with a uniform distribution of dimensionless parameter λ in the central zone, exhibited a localized crack forming at the midpoint, where the cross-section is at its smallest, as detailed in

Table 1, Table 2 and Fig. 14-c,f. In contrast, for specimens S11 and S12, which have a differing distribution of dimensionless

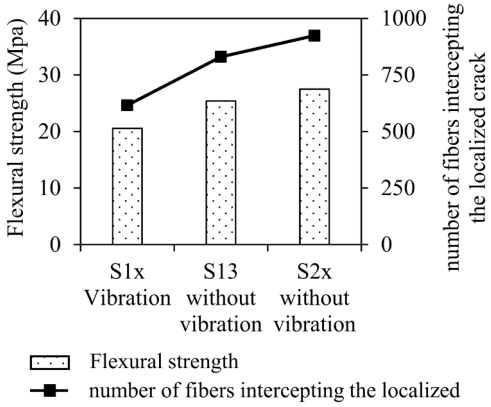

Fig. 20. The effect of the cross angle and the vibration on the measured flexural strength and the number of fibers intercepting the localized measured by image analysis.

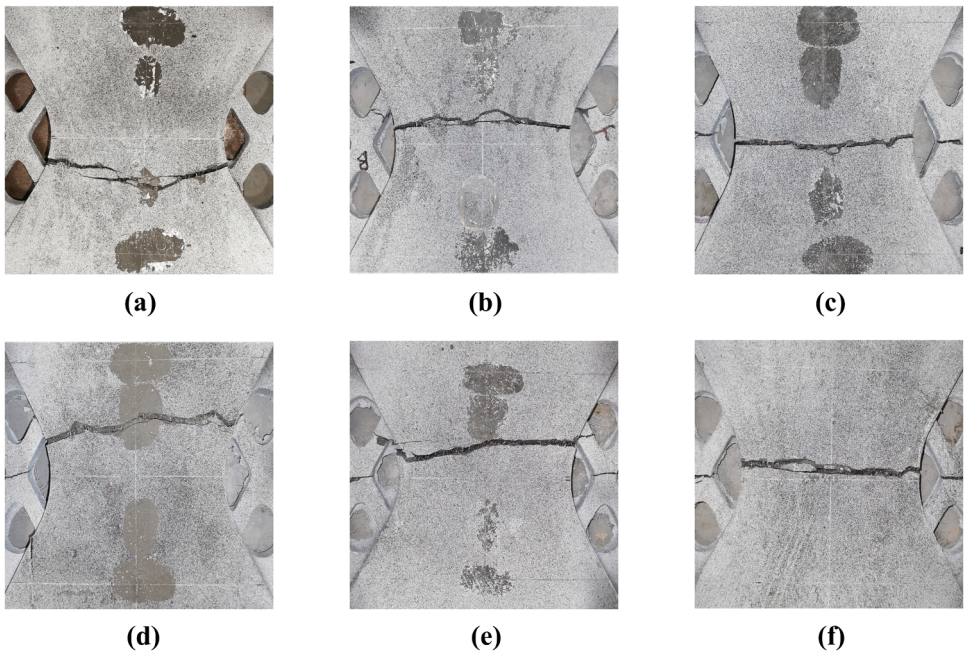

Fig. 21. Location of discrete softening cracks of specimens (a) S11; (b) S12; (c) S13; (d) S21; (e) S22; (f) S23.

parameter λ between the upper and lower sections, the localized crack forms at the boundary between these two areas (Fig. 14-a,b). A similar pattern was observed in specimen S22 (Fig. 14-d), where the localized crack developed in an area with fewer fibers. As highlighted in the image analysis results, an area with low fiber content was identified near the localized crack in specimen S21. This configuration facilitated the formation of a longitudinal crack and subsequent additional cracks, thereby enhancing the damage distribution and flexural strength of specimen S21.

4. Numerical modeling

4.1. FEM model parameters calibration

The geometry of the prototype X-connection specimens is discretized by an 8-node incompatible mode eight-node brick element (C3D8I) with a characteristic size equal to 15 mm. As a schematic representation, the center area includes 6 rows and 3 columns (from 6th to 11th row and from 4th to 6th column), which is determined by position corresponding with MIM (Fig. 22-a). The remaining areas have the same field variable (FV) equal to 1. The thickness of the specimen is 30 mm.

Fig. 22-b shows the FEM mesh of the bending test with X form specimen, two lower supports (one of them is fixed), and the

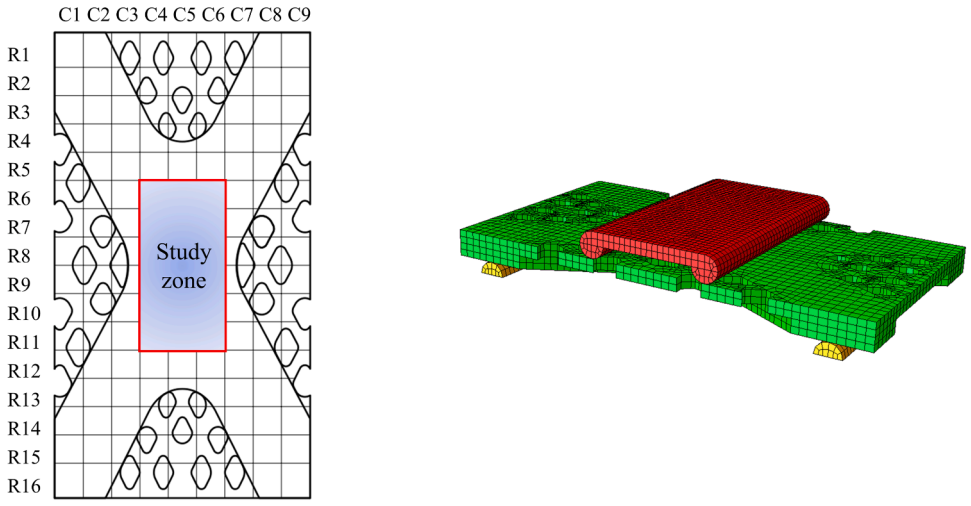

Fig. 22. (a) Diagram of 144 positions MIM (16 rows and 9 columns) and study zone (from 6th to 11th row and from 4th to 6th column); (b) FEM model.

displacement of the upper support is imposed with a closed-loop testing control. The support and UHPFRC specimens had "hard" contact in the normal direction and "penalty" with a friction coefficient equal to 0.3 in the tangential direction. The concrete material parameters used in this study are the modulus of elasticity E, the Poisson's ratio υ, and the CDP parameters for cracked concrete, which include: dilation angle ψ, shape factor K_c, stress ratio σ_{b0}/σ_{c0}, eccentricity, and viscosity parameter. Table 6 reports the values of CDP model parameters employed in this work which are similar to the ones employed in previous works on UHPFRC [41-43,50]. A preliminary analysis of varying mesh sizes demonstrated that in Abaqus CDP, finer mesh sizes increase the predicted flexural strength without appropriate numerical regularization. However, in this work, regularization was not necessary, as the chosen 15 mm mesh size aligned well with experimental results, with a relatively uniform mesh size applied across all elements. This configuration provided at least two finite elements through the thickness and ensured appropriate scale separation, exceeding the mean fiber embedded length of 6 mm, thus preserving model reliability without compromising continuum assumptions. Consequently, implementing numerical regularization, such as fracture energy-based scaling with element size, was unnecessary in this simplified analysis.

As detailed in previous work [19], the FEM model necessitates the estimation of a reference tensile law for uniformly aligned fibers, referred to here as Tensile Law Uniform (TLU-AI). This tensile law was directly estimated from a composite model based on fiber pull-out behavior [19] and was also compared with the estimate derived from inverse analysis of flexural tests in accordance with the SIA standard [18]. Given the satisfactory agreement between the laboratory tests and numerical models (Fig. 23), the TLU-AI has been reasonably accepted. The local tensile law was then calculated by scaling the TLU-AI law to the actual stress-strain relationship ($\sigma-\epsilon$) to each material point by using a field variable (FV) which is calibrated in function of fiber volume V_f and fiber orientation α locally measured at the by the Magnetic Inductance Method (MIM). Based on the actual fiber distribution in the material point as measured by MIM, the local tensile law will be an intermediate case between the two bounds, the case of fiber orientation of 0°, considered the strongest scenario, and at 90°, which represents the weakest case. Fig. 23 compares the tensile laws for both orientations. This approach was applied and validated by Tran et al. [19] to predict the tensile response of five specimens characterized by varying fiber uniformity.

Table 6
The CDP model parameters employed for FE computation.

Elastic Parameter			
Young's Modulus (*)	50.5 GPa	Poisson's Ratio	0.2
Concrete Damage Plasticity (CDP) Parameters			
Plasticity		Compressive Behavior (**)	
Dilation Angle	56	Inelastic Strain	Yield Stress
Eccentricity	0.1	0	100 MPa
σ_{b0}/σ_{c0}	1.16	0.002	140 MPa
K	2/3	0.009	40 MPa
Viscosity Parameter	0.0001		
Mesh Type: C3D8I (incompatible mode eight-node brick element)			

* Average Young's modulus of the cement-based matrix and fiber.
** Compression strength measured on cylinders

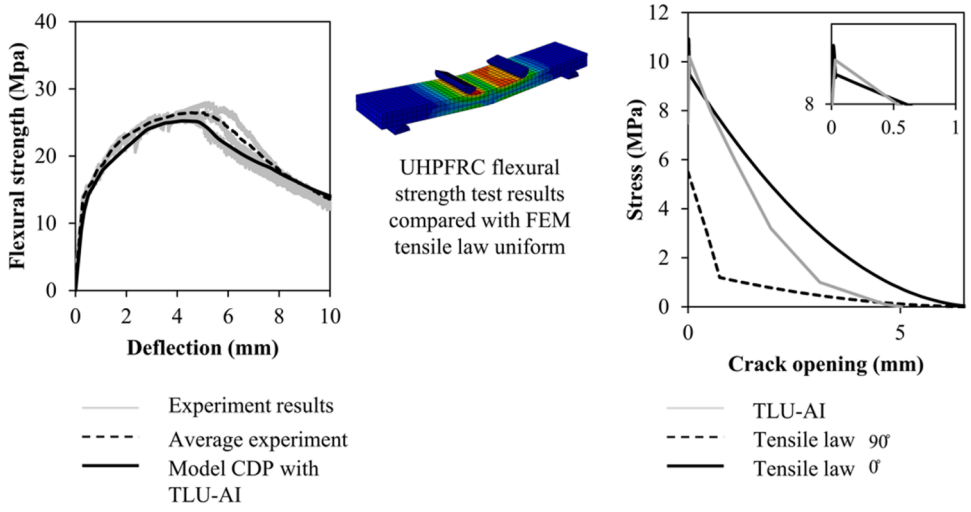

Fig. 23. (a) Comparison of simulated and experimental flexural test results; (b) The tensile behavior type displacement (stress vs. crack opening) of CDP model for fibers inclined of 0^0 and 90^0 with respect the tensile stress.

4.2. NLFEA simulation of the flexural response accounting for MIM measured fiber distribution

In the nonlinear finite element analysis (NLFEA) of the flexural response of X-specimens, it is essential to account for the actual fiber distribution. In this study, we focused on X-specimens S13 and S23, as their fiber distributions are similar in the vicinity of the localized crack, indicating that the measurements obtained from the Magnetic Inductance Method (MIM) and their differences are acceptable (see Table 5). Specimen S11, which also exhibits an acceptable difference, was not selected because the localized crack formed outside the central zone, resulting from a complex and uneven fiber distribution between the bottom and top sides due to extended vibration time.

Fig. 24-a shows the prediction of FEM with Tensile Law Uniformly from Analysis Inverse (TLU-AI), tensile law uniformly from tensile law local with $\mu_0 = 0.5$ and tensile law local of specimens S13 and S23. The model with the TLU-AI is overestimated compared

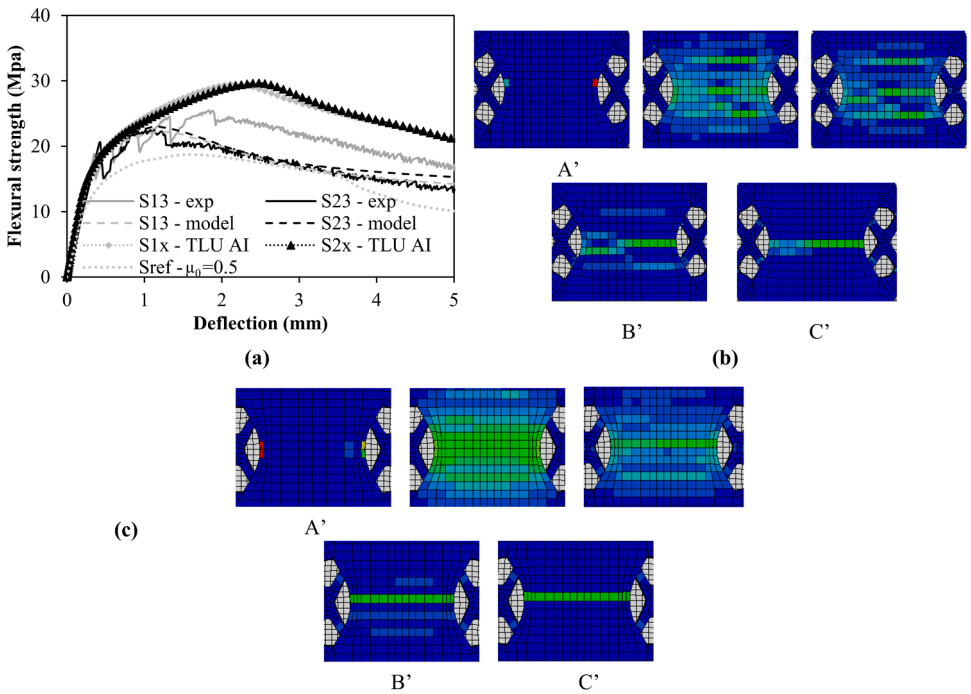

Fig. 24. (a) Prediction of FEM with TLU AI, tensile law uniformly from tensile law local with $\mu_0 = 0.5$ and tensile law local of specimen S13 and S23; (b) Fracture process S13 by FEM; (c) Fracture process S23 by FEM.

to the experimental results due to the lack of information about the distribution as well as the orientation of fiber. The use of this tensile law is for comparison between two versions of the specimen. Indeed, specimens from series S2x have a higher flexural strength at the fracture point M_{max} than specimens from series S1x, but the difference is not significant between the two specimen versions.

On the other hand, the model with the tensile law local is underestimated compared to the experimental of S13 and good agreement prediction of M_{max} with specimen S23. Fig. 24-b,c shows the fracture process of both specimens by NLFEA.

In specimen S23, the few micro-cracks occurred outside the central zone (Fig. 16-c with point B'). The prediction of fracture development seems to be better in specimen S13, the individual cracks in the model can be easily distinguished. With 5 % underestimation of the μ_0 as shown in Table 5, this result may explain why this specimen is not achieved the higher M_{max}. Thus, the complexity of the structure, as well as the limitation of the probe in terms of measurement area, are the causes of the inaccuracy of the model. Although a reasonable prediction cannot be made, MIM-FEM is a promising tool in controlling the quality of architectural UHPFRC elements with complex shapes where fiber distribution may be non-uniform in further study.

It is interesting to estimate the effect of fiber distribution on the flexural strength using a K-factor, similar to the approach in the AFGC (Association Française de Génie Civil) French design recommendations [12,51]. Consequently, we defined a K-factor for each beam as follows:

$$K^{def} = \frac{M_{\max}^{unif\_\mu_0=0.5}}{M_{\max}^{\exp}} \tag{7}$$

where $M_{\max}^{unif\_\mu_0=0.5}$ is the average flexural strength of the reference beam which a supposedly uniform fiber distribution with the fiber orientation factor $\mu_0 = 0.5$, $M_{\max}^{\exp}$ is flexural strength of each beam. We can also define the

$$K_{Local}^{def} = \frac{M_{\max}^{unif\_\mu_0=0.5}}{\min\left(M_{\max}^{\exp}\right)} \tag{8}$$

$$K_{Global}^{def} = \frac{M_{\max}^{unif\_\mu_0=0.5}}{\overline{M_{\max}^{\exp}}} \tag{9}$$

where $\min\left(M_{\max}^{\exp}\right)$ is the minimum value of the experimental results and $\overline{M_{\max}^{\exp}}$ is the average of the experimental results. Table 7 shows the results of K factor for the bending tests with the reference $M_{\max}^{unif\_\mu_0=0.5} = 18.72$ (MPa) which was estimated by NLFEA by considering a 3D fiber distribution (Fig. 24-a). As expected, the K-factor of specimen S12 is smaller than 1. If we consider all results, $K_{Local} = 1.06$ is greater than 1 meaning that the fiber distribution is important for such type of X-connection, which is S12 connection in specific. The fact that $K_{Global} = 0.75 < 1$ indicates that the fibers are distributed uniformly in a 2D manner due to the wall effect, which results in a flexural behavior superior to that of a uniformly oriented 3D distribution.

5. Conclusions

This case study seeks to investigate the impact of fiber distribution on the flexural behavior of X-connections, which are critical design elements in an innovative latticework UHPFRC footbridge concept. Based on the results obtained, the following conclusions can be drawn:

1. The fabrication process demonstrated that X-connections were successfully cast using fully recyclable wax formwork. The application of external vibration led to fiber segregation, which affected the mechanical performance of the X-connections S11 and S12.
2. The flexural strength and fracture energy of the X-connections were significantly correlated with the number of fibers bridging the main localized crack (Fig. 19-d) and were only slightly influenced by the changing the design of the X-connection shape, with the angle changing from 60° to 52° (Fig. 20).

Table 7
K factor for the bending tests.

Specimen	Flexural strength at the fracture point	Energy dissipated	$K = \frac{M_{\max}^{unif\_\mu_0=0.5}}{M_{\max}^{\exp}}$
	M_{max} (MPa)	W* (J)	
S11-exp	23.6	32.9	0.79
S12-exp	17.5	23.6	1.06
S13-exp	25.4	33.2	0.74
S21-exp	34.2	49.8	0.54
S22-exp	25.9	34.7	0.72
S23-exp	22.4	27.6	0.82
Model with TLU AI – S1x	29.5	n.a.	0.63
Model with TLU AI – S2x	29.6	n.a.	0.63

W*: energy dissipated up to 7 mm of deflection.

3. The use of the MIM non-destructive testing (NDT) method on complex UHPC geometries like the X-connection showed some limitations, as indicated by the low correlation between the fiber orientation factor μ_0 from MIM and that from image analysis of the cracked section (Fig. 19-c). These differences are likely due to the limited volume measured by the MIM sensor, which may be influenced by edge effects and voids.
4. The X-connection shape typically led to a localized crack in the central zone, with limited development of multiple microcracks due to stress concentration. When fiber distribution promoted crack formation outside the central zone (Fig. 14.d), such as in specimen S21 (Fig. 16.d), multiple cracks formed, and ductility was improved. This suggests that ensuring ducitlity (or the formation of multiple microcracks) in zones with complex shapes and high stress concentration may require either a higher degree of fiber uniformity or an increased fiber volume if uniformity cannot be maintained..
5. The estimated fiber orientation factor K_{global} for the tested X-connections was similar to that of 2D uniform fiber orientation, confirming a preferential fiber alignment due to wall effects. Additionally, it was observed that external vibration resulted in an unfavorable orientation factor K_{local} exceeding 1 for specimen S12.
6. For specimens with satisfactory MIM measurements (S13 and S23), the NLFEA accurately replicated the flexural response in terms of moment-deflection. The X-connection induces stress concentration, promoting crack localization, favoring the formation of larger, visible cracks (Fig. 23-b). This corresponds with experimental results, where only specimen S21 exhibited significant multiple cracking due to optimal fiber alignment. Thus, a fiber volume content exceeding 1 % is recommended to ensure consistent microcracking and reduce early crack localization in X-connections under tensile stresses.
7. For specimens where MIM measurements were not affected by the connection geometry (S13 and S23), the NLFEA integrating MIM effectively replicated the observed flexural response in terms of moment-deflection. This confirms that only specimen S21 exhibited significant multiple cracking due to optimal fiber alignment. However, despite the favorable fiber orientation and changes in the angle of the X-connection shape, it is recommended that a fiber volume content exceeding 1 % be used for the casting method.

Future studies should investigate alternative casting methods, including pressurized flow or 3D printing, to improve fiber uniformity in complex shape elements as well as identify the minimum optimal fiber volume required to promote multiple cracking. Additionally, developing smaller probes for the Magnetic Inductance Method (MIM) is recommended to enhance accuracy and reliability when assessing fiber distribution in UHPFRC complex geometries.

CRediT authorship contribution statement

Luca Sorelli: Conceptualization, Formal analysis, Funding acquisition, Methodology, Project administration, Resources, Supervision, Writing – original draft, Writing – review & editing. **Duc Anh Tran:** Conceptualization, Data curation, Formal analysis, Investigation, Methodology, Software, Validation, Visualization, Writing – original draft, Writing – review & editing. **Christian Dupuis:** Conceptualization, Data curation, Funding acquisition, Methodology, Supervision, Writing – original draft, Writing – review & editing. **Samuel Bernier-Lavigne:** Conceptualization, Formal analysis, Methodology, Visualization. **Sandrine Heroux:** Investigation, Methodology. **Mahdi Ben Ftima:** Formal analysis, Software, Conceptualization. **David Conciatori:** Funding acquisition.

Declaration of Competing Interest

On behalf of my co-authors, we confirm that there are no conflicts of interest regarding this manuscript.

Acknowledgements

We would like to the FRNQT strategic team program for financing the salary of the first author and part of the experimental expenses. We would also like to extend our gratitude to Genevieve Côté and Nicolas Gauvreau from Beton Génial (BPDL) for their support in casting the first series of specimens at their facility.

Annex 1

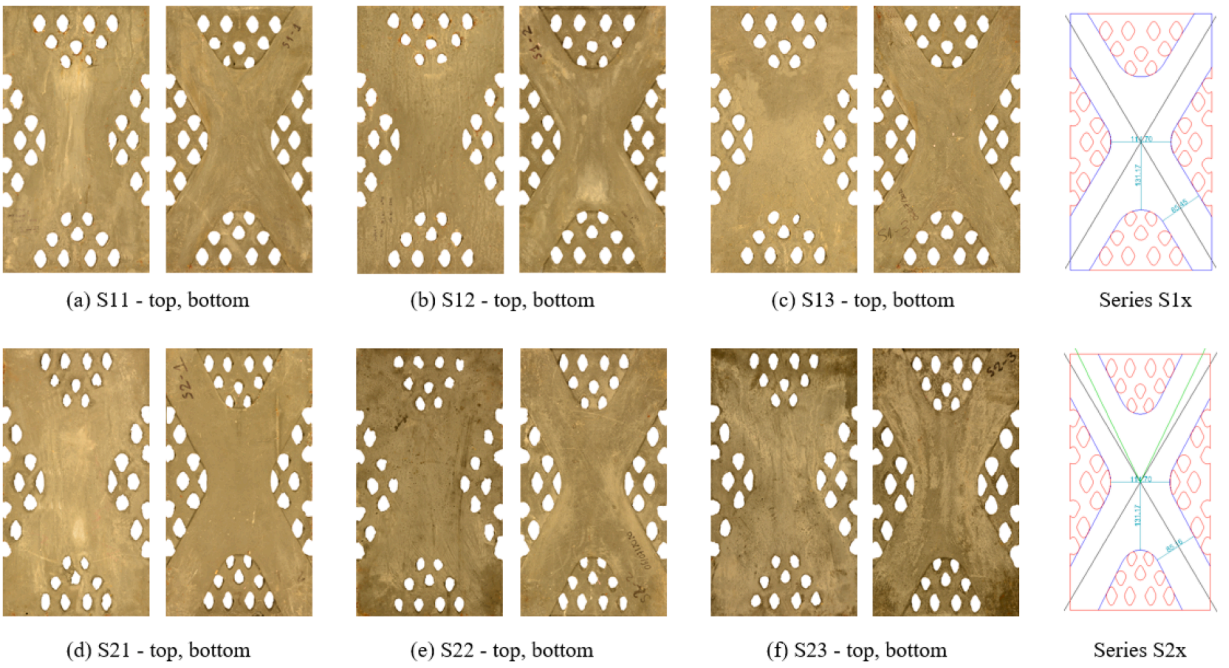

Fig. 25. Six prototypes for MIM and bending test (a) S11 – top, bottom; (b) S12 – top, bottom; (c) S13 – top, bottom; (d) S21 – top, bottom; (e) S22 – top, bottom; (f) S23 – top, bottom.

Data availability

Data will be made available on request.

References

[1] M. Mimram, M. Bonera, G. Barrau, and P. Mazzacane, Roofing of Montpellier—South of France TGV Station, in *Proc., Int. Conf. on Ultra-High Performance Fiber Reinforced Concrete*, 2017, pp. 837–856.
[2] P. Mazzacane, R. Ricciotti, G. Lamoureux, D. Corvez, Roofing of the stade Jean Bouin in UHPFRC", presented at the Symposium on ultra-high performance fibre-reinforced concrete, 87, RILEM, Marseille: RILEM PRO, Marseille, 2013, pp. 59–68.
[3] R. Ricciotti, J. Portelatine, F. Nicolas, Museum of European and Mediterranean Civilizations (MuCEM): High UHPFRC Content Structure Design, in: J. Resplendino, F. Toulemonde. (Eds.), Designing and Building with UHPFRC, John Wiley & Sons, 2013, pp. 487–500.
[4] P. Mazzacane, R. Ricciotti, F. Teply, E. Tollini, D. Corvez, MUCEM: The builder's perspective, Newsletter (2015).
[5] S. Aubry, et al., A UHPFRC cladding challenge: the fondation Louis Vuitton pour la création" Iceberg, Newsletter (2016).
[6] "⟨https://www.webofscience.com/wos/woscc/citation-report/b7abb61c-be58-4725-84c3-09ee16e6bfbe-6bcb6073?page= 1⟩."
[7] D. Géhin, E. Brühwiler, N.J. Bertola, L. Widmer, Design and Construction of the" Chaumény" Footbridge in Posttensioned UHPFRC. IABSE Symposium Prague 2022, IABSE, 2022, pp. 285–292. ⟨https://infoscience.epfl.ch/record/294780⟩. Accessed: Feb. 24, 2024. [Online]. Available:.
[8] D. Corvez, E. Ferrier, L. Michel, A. Ammouche, J.-P. Commène, Ultra-high performance concrete reinforced with stainless steel fibres: from material optimization to structural component response. Int. Symposium on UHPFRC, 2013. ⟨https://www.afgc.asso.fr/app/uploads/2014/01/pp-777-788-Corvez-1.pdf⟩. Accessed: Feb. 24, 2024. [Online]. Available.
[9] O. Bayard, Approche multi-échelles du comportement mécanique des bétons à ultra hautes performances renforcés par des fibres courtes, Ph.D. Thesis, Cachan, Ecole normale supérieure, 2003.
[10] G. Bernier, M. Behloul, Effet de l'orientation des fibres sur le comportement mécanique des BPR, Colloq. Int. Francoph. sur Les. bétons Renf. éS. De. Fibres M. éTall (1996) 233–240.
[11] M.A. Baril, et al., Effect of casting flow defects on the crack propagation in UHPFRC thin slabs by means of stereovision Digital Image Correlation, Constr. Build. Mater. 129 (2016) 182–192.
[12] A. Simon, D. Corvez, P. Marchand, Feedback of a ten years assessment of fibre distribution using K factor concept, UHPFRC 2013-Int. Symp. . Ultra-High. Perform. Fibre-Reinf. Concr. (2013) 669–678.
[13] B. Vermeulen, UHPFRC in Architecture, TU Delft, Delft University of Technology, 2014.
[14] S. Nunes, M. Pimentel, F. Ribeiro, P. Milheiro-Oliveira, A. Carvalho, Estimation of the tensile strength of UHPFRC layers based on non-destructive assessment of the fibre content and orientation, Cem. Concr. Compos. 83 (Oct. 2017) 222–238, https://doi.org/10.1016/j.cemconcomp.2017.07.019.
[15] R. Valente, M. Pimentel, S. Nunes, Characterization of the anisotropic tensile response of ultra-high performance fibre reinforced cementitious composites, Struct. Anal. Des. (2020) 7.
[16] X. Shen, E. Brühwiler, Influence of local fiber distribution on tensile behavior of strain hardening UHPFRC using NDT and DIC, Cem. Concr. Res. 132 (Jun. 2020) 106042, https://doi.org/10.1016/j.cemconres.2020.106042.
[17] M. Pimentel, S. Nunes, Determination of the fibre content and orientation in UHPFRC layers using NDT–application to the simulation of the behaviour of strengthened beams, Maint. Monit. Saf. Risk Resil. Bridg. Bridge Netw. (2016).
[18] "SIA 2052, 'Béton fibré ultra-performant (UHFB) – Matériaux, dimensionnement et exécution. Projet final après mise en consultation,' Cahier technique, 2014."

[19] D.A. Tran, X. Shen, L. Sorelli, M. Ben Ftima, E. Brühwiler, Predicting the effect of non-uniform fiber distribution on the tensile response of ultra-high-performance fiber reinforced concrete by magnetic inductance-based finite element analysis, Cem. Concr. Compos. 135 (Jan. 2023) 104810, https://doi.org/10.1016/j.cemconcomp.2022.104810.
[20] R. Fabbri and D. Corvez, Rationalisaztion of complex UHPFRC façade shapes, in *Toutlemonde F., Resplendino J., eds. Proceedings of International Symposium on Ultra-High Performance Fiber-Reinforced Concrete. Marseille, France*, 2013, pp. 27–36.
[21] R. Fabbri, J. Principe, M. Leone, Exploring UHPFRC possibilities, UHPFRC, 2017.
[22] L. Sorelli, , 2022, A multidisciplinary case study of an Ultra High Performance Fiber Reinforced Concrete (UHPFRC) Footbridge.
[23] J. Orr, A. Darby, 2012, Flexible formwork for visual concrete.
[24] T. Wangler, et al., Digital concrete: opportunities and challenges, RILEM Tech. Lett. 1 (Oct. 2016) 67, https://doi.org/10.21809/rilemtechlett.2016.16.
[25] Sandrine Héroux, FABRICATION NUMÉRIQUE ET COFFRAGES COMPLEXES: générer l'architecture non standard en bfup avec les nouvelles technologies,
[26] B.A. Graybeal, 2006, Material property characterization of ultra-high performance concrete, 2006.
[27] B. Graybeal, Development of non-proprietary ultra-high performance concrete for use in the highway bridge sector, Turn. -Fairbank Highw. Res. Cent. Fed. Highw. Adm. (2013).
[28] M. Berry, Feasibility of Non-Proprietary Ultra-High Performance Concrete (UHPC) for use in Highway Bridges in Montana (January), Mont. Dep. Transp, 2015.
[29] "'Fonctions de Rhino 6,' Rhino3D, consulté le 21 octobre, 2019, ⟨https://www.rhino3d.com/6/features⟩."
[30] "'RhinoCAM,' MecSoft, consulté le 21 octobre, 2019, ⟨https://mecsoft.com/rhinocam/⟩."
[31] J. Mainka, H. Kloft, S. Baron, H.-W. Hoffmeister, K. Dröder, Non-waste-Wachsschalungen: Neuartige Präzisionsschalungen aus recycelbaren Industriewachsen, Beton- Stahlbetonbau 111 (12) (Dec. 2016) 784–793, https://doi.org/10.1002/best.201600055.
[32] S. Héroux and d'art et de design Université Laval. Faculté d'aménagement d'architecture, *Coffrer. Recycler. Réutiliser. Coffrages complexes en cire réutilisable informés par simulations acoustiques et algorithmes génétiques*. in Collection Mémoires et thèses électroniques. Université Laval, 2020. [Online]. Available: ⟨https://books.google.ca/books?id=ZVDUzQEACAAJ⟩.
[33] J.P. Vincler, Effet de la migration accélérée du chlore sur la durabilité des BFUP, Maîtrise En. G. énie Civ., Univ. é Laval, Québec (2018).
[34] "*Read image from graphics file - MATLAB imread*". *[Online*]. *Available*: ⟨https://www.mathworks.com/help/matlab/ref/imread.html?searchHighlight=imread⟩ &s_tid=doc_srchtitle.
[35] *"Convert image to binary image, based on threshold - MATLAB im2bw". [Online]. Available:* ⟨https://www.mathworks.com/help/images/ref/im2bw.html?searchHighlight=im2bw⟩ *&s_tid=gn_loc_drop*.
[36] B. Mlekusch, Fibre orientation in short-fibre-reinforced thermoplastics II. Quantitative measurements by image analysis, Compos. Sci. Technol. 59 (4) (Mar. 1999) 547–560, https://doi.org/10.1016/S0266-3538(98)00101-8.
[37] C. Eberhardt, A. Clarke, Fibre-orientation measurements in short-glass-fibre composites. Part I: automated, high-angular-resolution measurement by confocal microscopy, Compos. Sci. Technol. 61 (10) (Aug. 2001) 1389–1400, https://doi.org/10.1016/S0266-3538(01)00038-0.
[38] M. Bastien-Masse, E. Denarié, E. Brühwiler, Effect of fiber orientation on the in-plane tensile response of UHPFRC reinforcement layers, Cem. Concr. Compos. 67 (Mar. 2016) 111–125, https://doi.org/10.1016/j.cemconcomp.2016.01.001.
[39] J. Aveston, A. Kelly, Theory of multiple fracture of fibrous composites, J. Mater. Sci. 8 (3) (Mar. 1973) 352–362, https://doi.org/10.1007/BF00550155.
[40] J. Wuest, E. Denarié, E. Brühwiler, L. Tamarit, M. Kocher, E. Gallucci, Tomography analysis of fiber distribution and orientation in ultra high-performance fiber-reinforced composites with high-fiber dosages, Exp. Tech. 33 (5) (Sep. 2009) 50–55, https://doi.org/10.1111/j.1747-1567.2008.00420.x.
[41] L. Chen, B.A. Graybeal, Modeling structural performance of ultrahigh performance concrete i-girders, J. Bridge Eng. 17 (5) (Sep. 2012) 754–764, https://doi.org/10.1061/(ASCE)BE.1943-5592.0000305.
[42] M. Shafieifar, M. Farzad, A. Azizinamini, Experimental and numerical study on mechanical properties of ultra high performance concrete (UHPC), Constr. Build. Mater. 156 (Dec. 2017) 402–411, https://doi.org/10.1016/j.conbuildmat.2017.08.170.
[43] R. Solhmirzaei, V.K.R. Kodur, Modeling the response of ultra high performance fiber reinforced concrete beams, Procedia Eng. 210 (2017) 211–219, https://doi.org/10.1016/j.proeng.2017.11.068.
[44] R. Soltanmohammadi, S. Iraji, T.R. de Almeida, M. Basso, E.R. Munoz, A.C. Vidal, Investigation of pore geometry influence on fluid flow in heterogeneous porous media: A pore-scale study, Energy Geosci. 5 (1) (2024) 100222.
[45] B. Dadmand, H. Sadaghian, S. Khalilzadehtabrizi, M. Pourbaba, M. Shirdel, A. Mirmiran, Studying the compressive, tensile and flexural properties of binary and ternary fiber-reinforced UHPC using experimental, numerical and multi-target digital image correlation methods, Case Stud. Constr. Mater. 18 (2023) e01865.
[46] J.G. Van Mier, Fracture processes of concrete, CRC press, 1996.
[47] H. Huang, X. Gao, K.H. Khayat, Contribution of fiber alignment on flexural properties of UHPC and prediction using the Composite Theory, Cem. Concr. Compos. 118 (Apr. 2021) 103971, https://doi.org/10.1016/j.cemconcomp.2021.103971.
[48] L. Teng, W. Meng, K.H. Khayat, Rheology control of ultra-high-performance concrete made with different fiber contents, Cem. Concr. Res. 138 (Dec. 2020) 106222, https://doi.org/10.1016/j.cemconres.2020.106222.
[49] "⟨https://zenodo.org/record/1433776#.Y9CgBHbMJEY⟩."
[50] V. Birtel, P. MarkParameterised finite element modelling of RC beam shear failure, in ABAQUS users' conference2006.
[51] AFNOR, Bétons - Bétons fibrés à ultra hautes performances - Spécification, performance, production et conformité, NF P18-470 Juillet 2016.